Ph.D. DISSERTATION

Experimental Investigations of Nanoelectrokinetic Phenomena through Novel Perm-selective Media

다양한 이온선택성 투과막에서의 나노전기수력학적 현상에 대한 실험적 검증

August 2020

DEPARTMENT OF
ELECTRICAL AND COMPUTER ENGINEERING
COLLEGE OF ENGINEERING
SEOUL NATIONAL UNIVERSITY

Sungmin Park

Experimental Investigations of Nanoelectrokinetic Phenomena through Novel Perm-selective Media

지도 교수 김 성 재

이 논문을 공학박사 학위논문으로 제출함
2020 년 8 월

서울대학교 대학원
전기 · 컴퓨터 공학부
박 성 민

박성민의 공학박사 학위논문을 인준함
2020 년 8 월

위 원 장 ____________________(인)
부위원장 ____________________(인)
위 원 ____________________(인)
위 원 ____________________(인)
위 원 ____________________(인)

Abstract

Perm-selective media has been widely used in various applications such as desalination, electro dialysis and battery, etc. In addition, micro-/nano-electrokinetic phenomena near the permselective media have been intensively studied. In many studies, material or geometry of the perm-selective media were adjusted for the easy fabrication or the new physics. In this thesis, material of the permselective media was adjusted by using ionic hydrogel and bio-based material, and also geometry of Nafion membrane was adjusted to have an undulation shaped surface. So the thesis was divided into two parts, one is the adjusting material, and the other is the adjusting geometry.

In Chapter 2, ionic hydrogel was introduced for capillarity ion concentration polarization (CICP). To overcome a world-wide water shortage problem, numerous desalination methods were developed with state-of-the-art power efficiency. However, a natural plant, mangrove can survive in salty environment with optimal power sources. As motivated by the desalting function of mangrove, here we proposed a spontaneous desalting mechanism, CICP. An ion depletion zone was spontaneously formed near a nanoporous material by the perm-selective ion transportation driven by the capillarity of the material, in contrast to an electrokinetic ion concentration polarization which achieves the same ion depletion zone by an external dc bias. This CICP device was shown to be capable of reduced an ambient flourecent signal more than 90% without any external electrical power sources. These results indicated that the CICP system can offer unique and economical approaches for a power-free water purification system.

In Chapter 3, biodegradable materials originated from well-known organisms such as human nail plate were rigorously investigated as a role of permselective nanoporous membrane. Most of nanofabrication methods are sophisticated and expensive due to the requirement of high class cleanroom facilities, while low-cost and biocompatible materials have been already introduced in the microfluidic platforms. Thus, an off-the-shelf and biodegradable material for those nanostructures can complete the concept of an eco-friendly micro/nanofluidic platform. A simple micro/nanofluidic device integrated with such materials was fabricated. Distinctive evidences (visualization of ion concentration polarization phenomenon, ohmic/limiting/overlimiting current behavior and surface charge-governed conductance) would fulfill the requirements of functional nanostructures for the nanofluidic applications. Therefore, this bio-based material, nail plate, would be utilized as a one of key elements of the biodegradable and eco-friendly micro/nanofluidic applications.

In chapter 4, micro/nano fluidic platform involving undulated surfaced Nafion membrane was investigated for the study of electrokinetic effect depending on the characteristic length scale of the system. Although the several studies have shown that overlimiting current was enhanced due to undulation surface at the long characteristic length (~O(100) mm), there are few studies that have shown undulation effect at the short characteristic length (~O(10) mm). In this chapter, we compared the undulation effect at two characteristic length of 15 mm and 150 mm. I-V characteristics were obtained at both 15mm and 150 mm and investigated the possibility of suppressing the undulation effect according to the depth of the device.

In this thesis, experimental investigation of the nanoelectrokinetic phenomena through novel perm-selective media was introduced. In chapter 2, 3, material of perm-selective media was adjusted by ionic hydrogel or bio-based materials and in chapter 4, geometry of the conventional perm-selective media, nafion, was modified to reveal the new physics.

Keyword : Ion concentration polarization, Perm-selective media, Ionic hydrogel, Human nail plate, Capillarity, Undulated surface.

Student Number : 2013-20791

Table of Contents

List of Figures

List of Tables

Chapter 1. Introduction

1.1 Permselectivity of the nanoporous membrane

In micro/nano fluidic systems, interesting properties that are not observed in bulk fluidic systems appear. This is because the lower the characteristic dimension of the fluid channel, the stronger surface force rather than the body force. In micro/nanofluidic regime, surface charge, surface tension and surface slippage, etc. are as dominant as gravitation and electrostatic force, etc.

For instance, in microchannel, when an electric field is applied to both ends of the microchannel that contains aqueous ionic solution, unlike in a bulk channel, electro osmotic flow appears due to surface charge of the channel wall. More precisely, the surface charge of the channel wall causes oppositely charged region of counter ions in the aqueous ionic solution to maintain charge neutrality of the solid-liquid interface. This screening region is called as the electrical double layer (EDL). When an electric field is applied to the fluid, the net charge of the EDL is moved by the generated Coulomb force. The resulting flow is called electric osmostic flow.

The EDL is divided into two layers according to the Gouy-Chapman-Stern model as shown in Figure 1.1: one is the stern layer and the other is the diffuse layer. In stern layer, counter ions are immobile and adsorbed near the wall surface. In diffuse layer, counter ions are able to move freely. The EDL distribution can be expressed using the Poisson-Boltzmann equation and the Debye-Huckel approximation. By using that, thickness of the EDL is characterized by Debye length (λ_d)as

$$\lambda_d = \left(\frac{\varepsilon_0 \varepsilon_r k_B T}{e^2 \sum_i n_i^\infty z_i^2} \right)^{1/2} \tag{1}$$

Where ε_0 is permittivity of free space, ε_r is relatively permittivity, k_B is the Boltzmann constant, T is absolute temperature, e is elementary charge, z_i^2 is the valence of ith ion and n_i^∞ is bulk concentration of ith ion [1].

The permselectivity appears as the dimension of channel decreases close to the Debye length. As shown in Figure 1.2(a) EDLs on both side of the channel do not overlap in the microchannel and the electrical potential at the center of the channel is zero. However, when the characteristic length scale of channel is close to the Debye length, and if channel is negatively charged, EDLs on both side of the channel overlap and the negative electric potential is maintained in every point of the channel as shown in Figure 1.2 (b). Therefore, the negative electric potential allows selective passage of cations through the channel. This counter-ion selective transportation called as permselectivity.

Permselectivity of the nanoporous membrane is understandable from the following Donnan equilibrium theory. In the case of the cation selective membrane and 1:1 electrolyte solution, concentration of the cation and anion inside the membrane is as follow.

$$\overline{c_+} = \frac{1}{2}\left(\sqrt{\overline{c_R} + 4c^2} + \overline{c_R} \right) \tag{2}$$

$$\overline{c_-} = \frac{1}{2}\left(\sqrt{\overline{c_R} + 4c^2} - \overline{c_R} \right) \tag{3}$$

Where $\overline{c_+}$ is cation concentration inside the membrane, $\overline{c_R}$ is concentration of wall of membrane, c is bulk concentration outside the membrane, $\overline{c_-}$ is anion

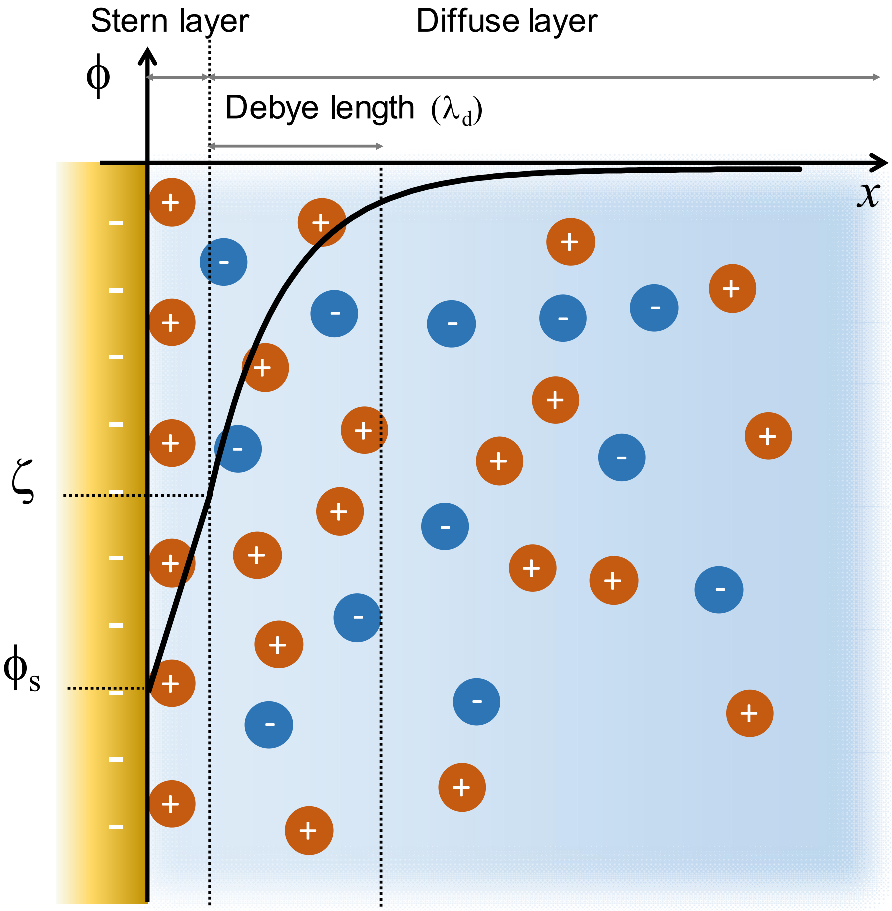

Figure1.1 Schematic image of electricaldouble layer

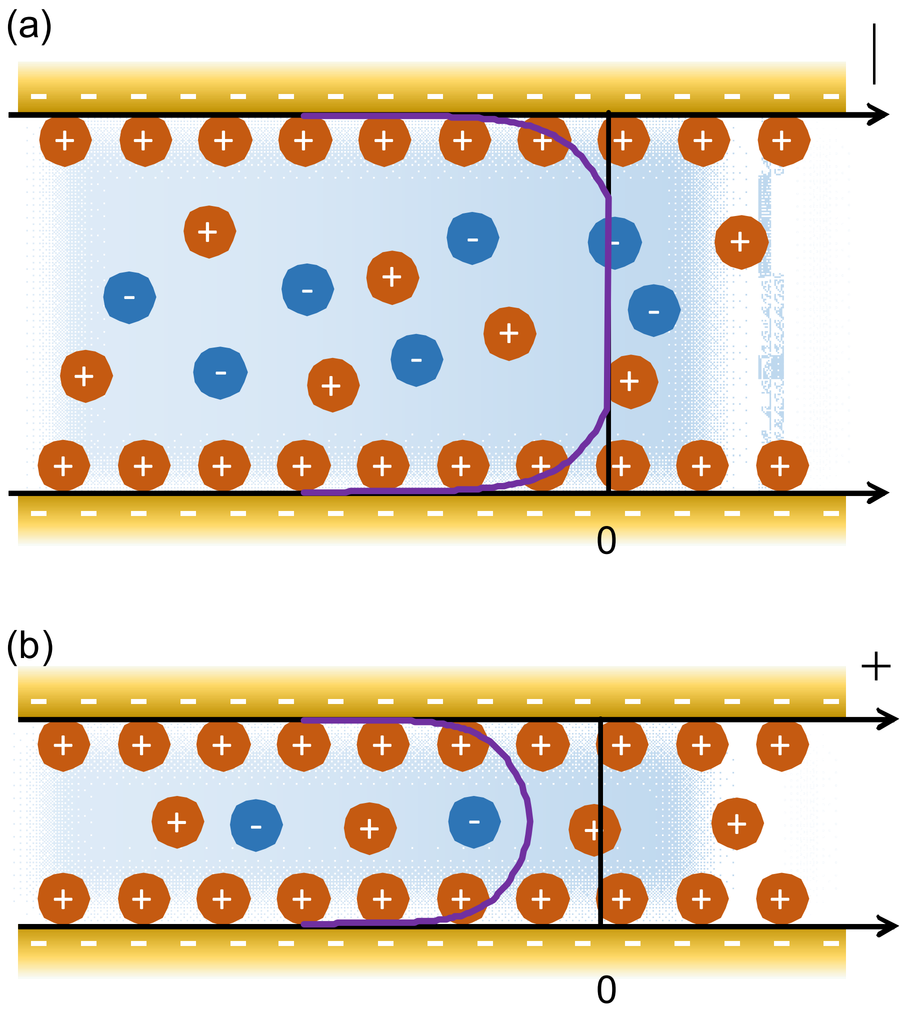

Figure 1.2 schematic image of electrical double layer (a) in microchannel and (b) in nanochannel

concentration inside the membrane.

In the case of the sodium chloride, the concentration ratio $\overline{c_{Cl}} / \overline{c_{Na}}$ ($\overline{c_{Cl}}$ is concentration of Cl^- inside the membrane and $\overline{c_{Na}}$ is concentration of Na^+ inside the membrane) is represented by $\overline{c_R}$ of membrane and c [2]. $\overline{c_{Cl}} / \overline{c_{Na}}$ decreases with c toward 0 as shown in Figure 1.3 (a) it is because Debye length of the membrane increases with c toward 0. This means that more overlapped Debye length introduces stronger perm selectivity. In Figure 1.3 (b), $\overline{c_{Cl}} / \overline{c_{Na}}$ represented by $\overline{c_R}$. $\overline{c_{Cl}} / \overline{c_{Na}}$ decreases with $\overline{c_R}$ increases and it means that the higher $\overline{c_R}$ attracted more cations, resulting in a high perm selectivity.[2]

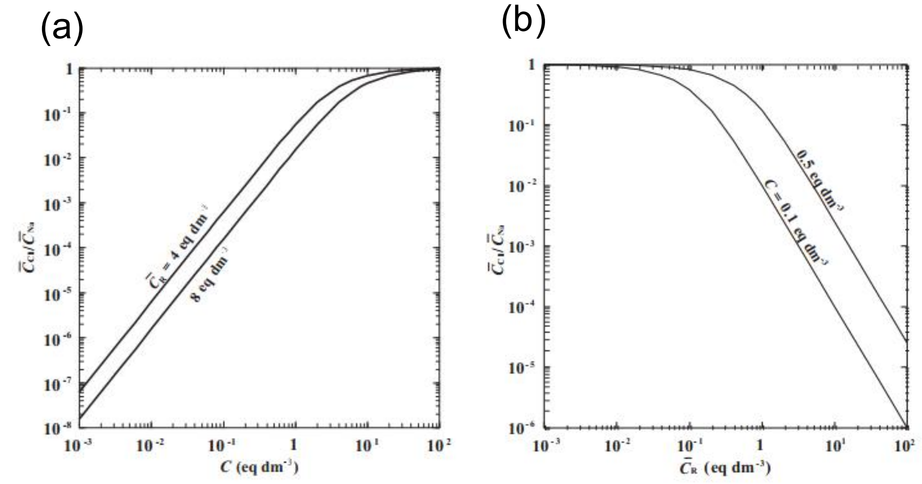

Figure 1.3 (a) Relationship between NaCl concentration in a solution and Cl-/Na+ ratio in cation exchange membrane and (b) Relationship between ion exchange group concentration and Cl-/Na+ratio in a cation exchange membrane. [2]

1.2 Examples of permselective structures

1.2.1 Ion exchange membrane

Ion exchange membrane is one of the most conventional membrane that has been used as permselective structure. Ion exchange membranes are composed of immobilized ion-functionalized groups and movable counter-ions. Depending on the type of ionic group, ion exchange membrane divided into two membrane, one is the cation exchange membrane and another is the anion exchange membrane. The ion-functionalized groups attached to the ion exchange membrane dissociated in the solution and released the counter-ions. The cation exchange membrane has functional groups such as a sulfonic acid, phosphoric acid and carboxylic acid group. In the case of the anion exchange membrane, ammonium cations, imidazole cations, and guanidinium cations are generally attached into the polymer backbones to obtain anion exchange membrane.

1.2.2 Nafion

Nafion is a brand name discovered by DuPont in the late 1960s [3] and it is sulfonated tetrafluoethylene based fluoropolymer-copolymer. When the membrane is immersed in aqueous ionic solution, proton is dissociated from sulfonic acid group. Negatively charged sulfonate group of Nafion introduce permselectivity. Nafion is highly conductive to cations and it suitable for a broad range of applications.

One of the uses of the Nafion is to produce chlorine and sodium/potassium hydroxide. Modern production methods produce these chemical from electrolysis of brine using a Nafion membrane between half-cells. Before the use of Nafion, mercury and asbestos had been used for producing chlorine and sodium/potassium hydroxide, and this method has disadvantage of worker safety and environmental concern. Nafion was the one of the solution for these problems. Another uses of the Nafion is membrane of the fuel cells. Nafion permit proton transport while preventing electron conduction so that the Nafion was found effective as a membrane for proton exchange membrane. In micro/nanofluidics Nafion is used for novel permselective membrane in ion concentration polarization applications which is explained in section 1.3 [4-7]

1.2.3 Synthetic hydrogel

Synthetic hydrogels can be attractive elements to perm-selective membrane due to their response to specific stimuli, such as pH or temperature change. [8, 9] the strong advantage of the hydrogels as a permselective membrane is that the properties of hydrogel are controllable by monomer composition and cross-linker density. In proper monomer composition and cross-linker density, pore size of hydrogel matrix becomes comparable to the Debye length. Fixed charged groups of the hydrogel generate negative potential and it makes hydrogels permselective. By controlling the polarity of the charged monomers, one can easily synthesize cation or anion selective membrane.[10]

1.2.4 Lithographically defined nanochannels

To fabricate well-defined nanochannel, lithographical methods have been used such as optical lithography, electron beam lithography and focused ion beam lithography. These methods are relatively sophisticated and expensive in high-class clean room facility, but they can fabricate nanochannels at the exact location and at the correct size. The basic principle of electron/focused ion beam lithography is simple: electron/ion sensitive resist cover the wafer and desired pattern is reproduced by scanning of focused beam of electrons/ions. This scanning process is very similar to what happens in an electron microscope, but only the video scanning has been replaced by computer scanning. In the case of the focused ion beam, it can be used in a wide range of applications due to their high mass compared with electrons.

Soft lithographical methods with minimal usage of cleanroom have accelerated the advances of nanofluidics studies and applications due to its cost and time efficiency [11, 12]. Especially, elastomeric material-based lithography is one of the easiest way to fabricate the nanostructure. For example, nanochannel can simply be created by roof-top collapse of elastomeric poly-dimethylsiloxane (PDMS) microchannel16. Similarly, when PDMS was covered micro-patterned substrate, triangular nanochannels were created at both sides of the micro-pattern [13, 14]

1.2.5 Others

Recently, many other researches have showed fabricating nano structures in various ways. Bio-based materials as a perm-selective membrane are one of those efforts. Chen *et al.* fabricated nano structured membrane using balsa wood samples[15]. Natural wood was compressed to convert from micro-sized cellulose channels to nano-sized channels and surface charge was modulated by etherification. This method has great advantage of biodegradability with an low-cost fabrication. Another example of the bio-based material is human nail plate and it is described in chapter 3. Self-assembled bead packing is another example of the fabricating nano structures. [16] Sub-micro sized particle (< 1μm) was used for bead and bead was assembled with face centered cubic structure. By the changing the polarity of the beads, polarity of structure was changed. This method has great advantage of the low-cost fabrication while the beads are weakly bonded with each other, so the membrane is very brittle.

1.3 Ion Concentration Polarization (ICP)

When the perm-selective membrane separates two channels containing a aqueous ion solution and an electrical field is applied between the two channels, unique phenomena called ICP occur. In the case of the cation-selective membrane, cations pass through the membrane while anions are blocked near the anodic side of the membrane. Therefore, the cations depleted near the anodic side of membrane. To satisfying charge neutrality, anions of anodic side of membrane repel from the perm selective membrane. At the cathodic side of the membrane, cations accumulate near the cathodic side of membrane and anions also accumulate to satisfying the charge neutrality. As shown in Figure 1.4, ion depletion region is developed near the anodic side of the membrane, and ion enrichment region is developed near the cathodic side of the membrane.

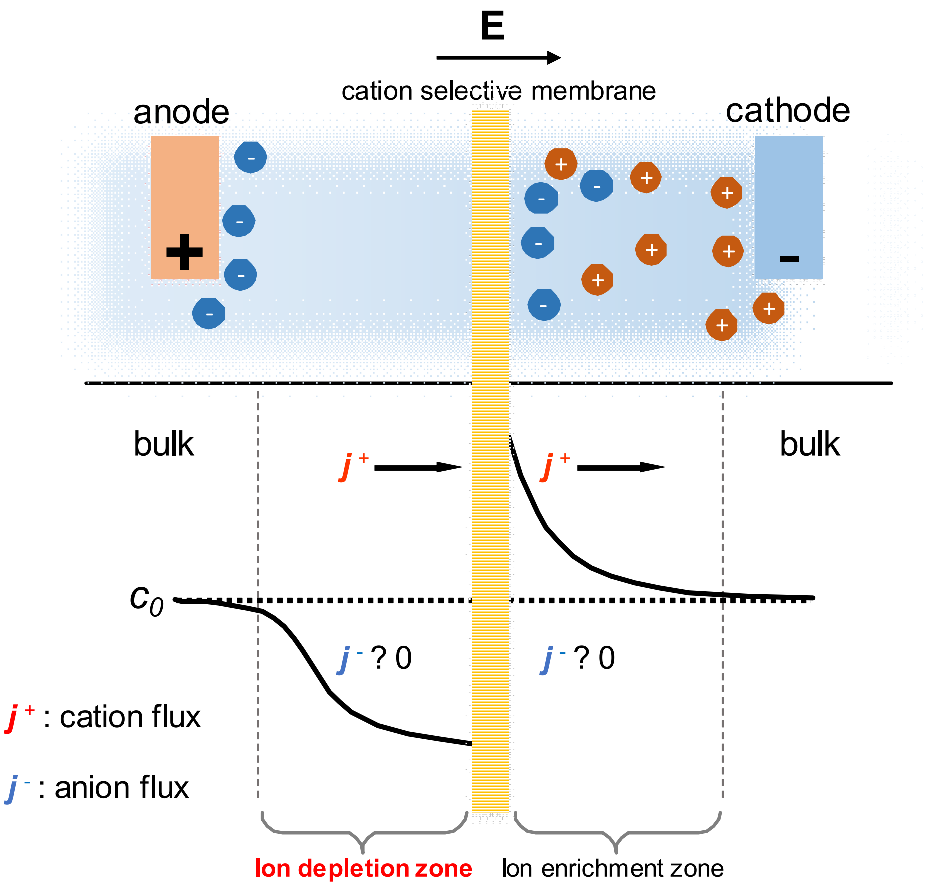

Figure 1.4 schematic image of the ion concentration polarization

Chapter 2. Ionic Hydrogel Membrane for Capillarity based Ion Concentration Polarization

2.1 Introduction

Recent noteworthy investigations in micro/nanofluidic devices enables to develop not only various biomedical but also significant energy and environmental applications1. Among these groundbreaking technologies, micro/nanofluidic platforms have successfully served as the differential shells of macro scale water purification / desalination systems [17-19]. One can microscopically investigate the salt separation mechanism occurring adjacent to nanoporous membranes or porous electrodes by flow field trackings or voltage-current measurements. While the state-of-the-art desalination methods, such as a reverse-osmosis and a flash distillation, can provide the gigantic amount of fresh water with a high energy efficiency[20], a low energy efficiency of small scale platforms and the requirement of high cost infrastructures have become acute nuisances, especially for remote / rural areas of the world. On the other hand, the micro/nanofluidic differential shells can be scalably integrated to a portable-scale system for individual usage or even to a mid-scale system for small village supply.

For such small-sized desalination / purification applications, ion concentration polarization (ICP) has been recently introduced [17, 21-23] ICP indicates the polarization of electrolyte concentrations at the anodic and cathodic side of a perm-selective membrane under dc bias. Typical behavior is that the concentration is largely depleted at the anodic side (also known as an ion depletion zone) and enriched at the cathodic side (also known as an ion enrichment zone) in the case of a cation-selective membrane and vice versa [24]. In addition to nanoporous membranes,[10, 14, 25] bipolar electrodes[26, 27] and nanoporous particles[28, 29] have been reported for a new practical platform to generate ICP as well. Intensive researches have been conducted to explore its fundamental aspects such as the source of over-limiting current [30-32], the vortex generation[33-35] and related instability issues[36] and its novel engineering applicability such as biological sample preparations[11, 37] energy saving mechanism[38] and desalination applications[17, 27]. While ICP desalination method is unprecedentedly capable of extracting fresh water out of high salinity, biologically infected, or even heavy metal contaminated water, the necessity of a high external electrical power source[17, 19] is still the most critical hurdle to be overcome. Therefore, a new desalination mechanism that consumes minimum level of energy is highly demanded.

In nature, mangrove trees that grow in saline water along tropical or subtropical coasts are well known for their unique physiological responses to survive in highly saline environments without any external supply of mechanical, chemical or electric power.[39] The phenomenological observations[39] of mangrove so far have found that the sap from the root’s xylem has about 90% lower salinity than the external saline water by a reverse osmosis (RO) mechanism. Therefore, we are particularly interested in the mangrove’s ability to exclude salt without any external energy. Motivated by the fact that the mangroves contain nanoporous structure which resembles a RO or ultra-filtration membrane [39], we suggested a new spontaneous desalination mechanism by introducing the nanoscale electrokinetic and the hydrodynamic transportation of ions at the interfaces between the nanoporous structure and the saline environment. We visualized the ion movements that illustrate the new class of an ion depletion phenomenon. By utilizing dry ionic hydrogel, the effective ionic flux through the hydrogel was induced by the capillarity of the hydrogel itself, instead of an external electrical bias, so that we named the currently exploited process as the capillarity ion concentration polarization (CICP). Osmo-poro-elastic process due to the swelling of the hydrogel[40, 41] is excluded in this work by a mechanical confinement [42-44] within a microchannel to focus on the role of capillarity. Both analytical and numerical models were obtained to analyze the statics and dynamics of the spontaneous desalting mechanism in Appendix A. Since the mechanism does not involve any electrical power source, it offered significant merits in terms of a power consumption and a stable operation compared to the conventional ICP mechanism. Therefore, CICP mechanism can be applied to power-free and small scale (possibly portable) desalination / purification devices that would be particularly useful in remote / rural and disaster-stricken areas.

2.2 Materials and methods

2.2.1. Synthetic hydrogel as a permsective membrane

The hydrogel which was made of 2-hydroxyethyl methacrylate (HEMA) and acrylic acid (AA), a cross-linker (ethylene glycol dimethacrylate (EGDMA)), and a photoinitiator, (2,2-dimethoxy-2 phenyl-acetophenone (DMPA)) was synthesized. The synthesized hydrogel become negatively charged by releasing hydrogen ions from acrylic group and backbone. In the hydrogel structure, HEMA acts as a backbone and created nano-sized pores. For this reasons, synthesized hydrogel could be utilized as a permselective membrane for CICP.

2.2.2 CICP device fabrication

The main building block of the CICP system was polydimethyl-siloxane (PDMS) material as schematically shown in Figure 2.1. The final device (vi) consisted of two layers of PDMS blocks. Bottom was for microchannel filled with the ionic hydrogel and top was for microchannel to inject the saline water sample. Silicon masters were prepared using SU8 photoresist with the microchannel dimension of 400 μm (width) × 50 μm (depth) × 16 mm (length) for bottom PDMS block and 100 μm (width) × 15 μm (depth) × 10 mm (length) for top PDMS block. The PDMS blocks were fabricated as follows. The PDMS material (Sylgard 184 Silicone elastomer kit, Dow Corning, USA) mixed with a curing agent at 10:1 ratio was poured on the silicon masters that had a desirable microchannel pattern. Then the polymer solution was cured in an oven for 4 hours at 75 ^{o}C.

Detailed fabrication process from the first schematic was as follows. Firstly, (i) only the top PDMS for hydrogel mold was treated with oxygen plasma (CUTE-MP, Femto Science, Korea) for adhesion of the hydrogel and attached to a blank bottom PDMS piece. Then (ii) the microchannel was filled with a hydrogel precursor material consisting of HEMA and AA, a cross-linker (EGDMA), and a photoinitiator, (DMPA) at the weight ratio of 32.51 : 6 : 0.41 : 1.25 (named 5:1 hydrogel) or 32.51 : 18 : 0.41 : 1.25 (named 5:3 hydrogel)12. The ratio of HEMA to AA would have a significant effect on CICP phenomenon as discussed later. All the materials were purchased from Sigma-Aldrich. UV irradiation for 8 minutes at the dose of 225 mW/cm^2 (WUV-L50, Daihan Scientific, Korea) polymerized the hydrogel inside the microchannel and then (iii) the top PDMS block was detached from the bottom blank PDMS piece. The hydrogel inside the microchannel was initially brittle and stiff (dry state) but the hydrogel absorbed a solution so that the portion of hydrogel became flexible and tough as the CICP proceeded. Finally, (iv) the flipped PDMS block for hydrogel and the PDMS for saline water samples were

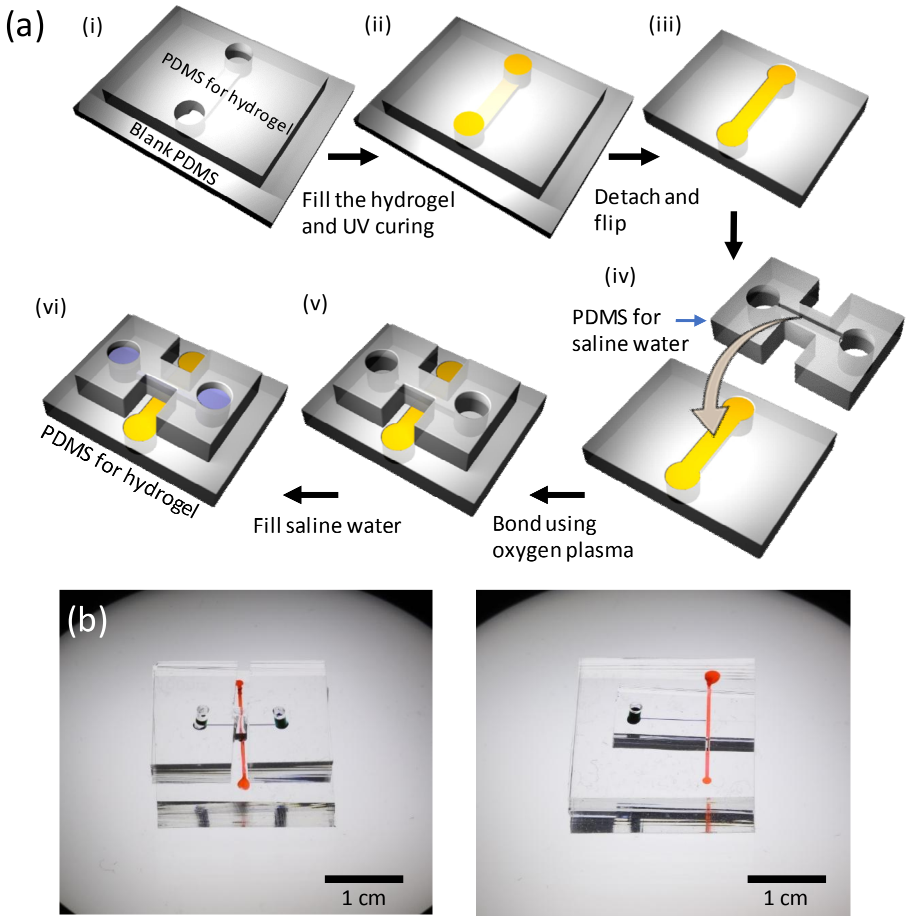

Center-connection device

End-connection device

Figure 2.1 The micro/nanofluidic CICP device. (a) The fabrication process of CICP system. (b) The photo of assembled CICP devices of the center-connection device and end-connection device.

irreversibly bonded with oxygen plasma treatment. Assembled devices placed on slide glass were shown in Figure 2.1 (b). There were two distinct designs, a “center-connection device” and an “end-connection device”. The center-connection device was designed for easiness of facilitating the experiment such as sample filling and flushing, while a residual flow was able to be completely eliminated in the end-connection device.

The microchannel inside top PDMS block was filled with KCl electrolyte solution at the concentration of 300 mM mixed with a fluorescent dye (Alexa 488, Sigma Aldrich, USA) for concentration tracking and negatively charged micro particles (d = 5 μm, Invitrogen, USA) for flow field tracking. KCl 300 mM was used for a simple theoretical interpretation by setting the same diffusivity of cation and anion and as the average salinity of brackish water.

2.2.3 Experimental setup

Compared to the conventional ICP process, no external voltage source was required for the present CICP system. Instead, the total experimental time took from a few hours to a few days depending on the device (c.f. a conventional ICP occurs within few seconds) so that the images of flow and concentration changes were captured every 2 minutes for few days using a commercial computer software (CellSens, Olympus, Japan) and an inverted fluorescent microscope (IX 53, Olympus, Japan). The location where the hydrogel channel and the sample channel crossed was intensively analyzed. A confocal microscope (FV1200, Olympus, Japan) was used for the 3-dimensional concentration profiling.

2.2.4 Concentration measurement from reference fluorescent signal

A microchannel which has the same dimension as used in the experiments is bonded to the glass to measure the reference intensity of florescence dye. The fluorescent dye (Alexa 488) is diluted with DI water at various concentrations. Each florescence dye solution is injected into the microchannel. Then the microscopic image of each solutions is captured and analyzed by a computer software (CellSens, ImageJ). Capture conditions are identical for each measurement. A plot of pixel intensity as a function of the concentration of fluorescent dye is obtained as shown in Figure 2.2. Then the unknown concentration can be determined using the plot by an interpolation.

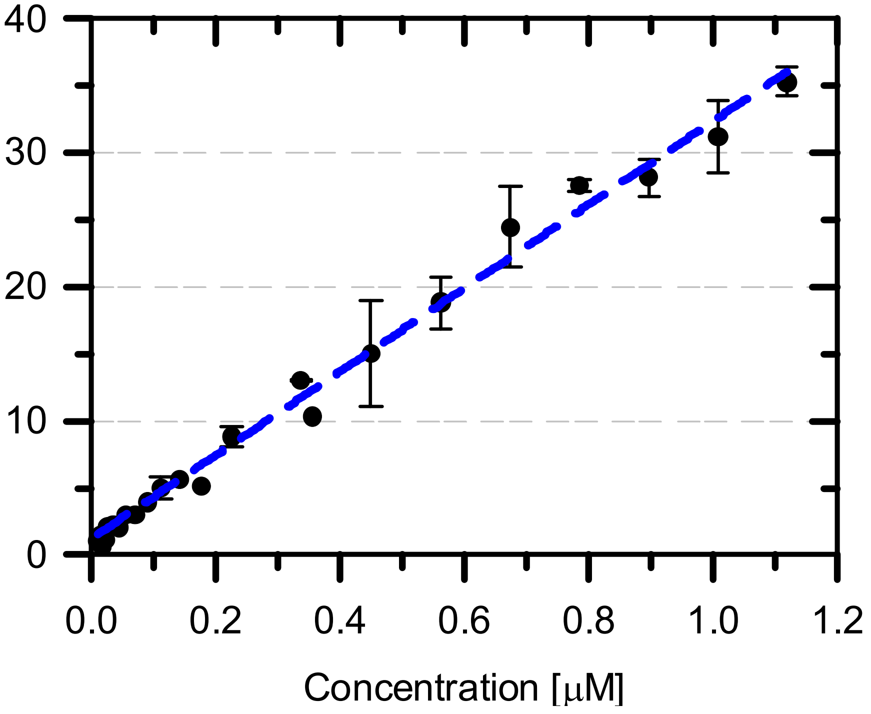

Figure 2.2 Reference fluorescent signal as a function of the dye concentration

2.3 Results and discussion

2.3.1 Imbibition rates through the ionic hydrogel

The ionic hydrogel is capable of absorbing ambient aqueous solution by capillarity. This phenomenon is critical to the presented CICP system, which utilized capillarity as a driving force for a liquid transportation. A hydrogel usually has an osmo-poro-elastic effect due to a significant swelling. However, the swelling was minimized by a mechanical confinement[42-44]. In this work, the hydrogel swelled within a microchannel and, thus, we were able to analyze the CICP phenomenon only by the capillarity effect. As shown in Figure 2.3 (a), there were two significant evidences of the imbibition by capillarity. Micro-particles were injected near the hydrogel pad and their motions were captured at distinct time intervals. As indicated, their paths converged toward the hydrogel pad from both reservoirs in the center-connection device, evidencing a mass sink at the center. In addition, as shown in Figure 2.4, microparticles of diameter= 1 μm went toward the hydrogel and the imbibition front gradually expanded as a function of time in end-connection device. Since there were no external driving forces (such as gravity or external electric / magnetic / acoustic field) other than the capillary force, the total volume that had disappeared (V_{water}) was calculated by the speed of the particles. Since we confirmed that there was no leakage at the bonding or hydrogel interfaces, the entire V_{water} should be transported into the hydrogel. Because the hydrogel has auto-fluorescence and it disappears when in contact with water molecules, the wetted volume of hydrogel (V_{wet}) was able to be measured by the progression of an imbibition front. Therefore, the fraction of these two volumes (V_{water}/V_{wet}) were the same as the porosity of the hydrogel and it was calculated to be around 0.1 which would be used as one of the important parameters in the aforementioned theoretical calculations.

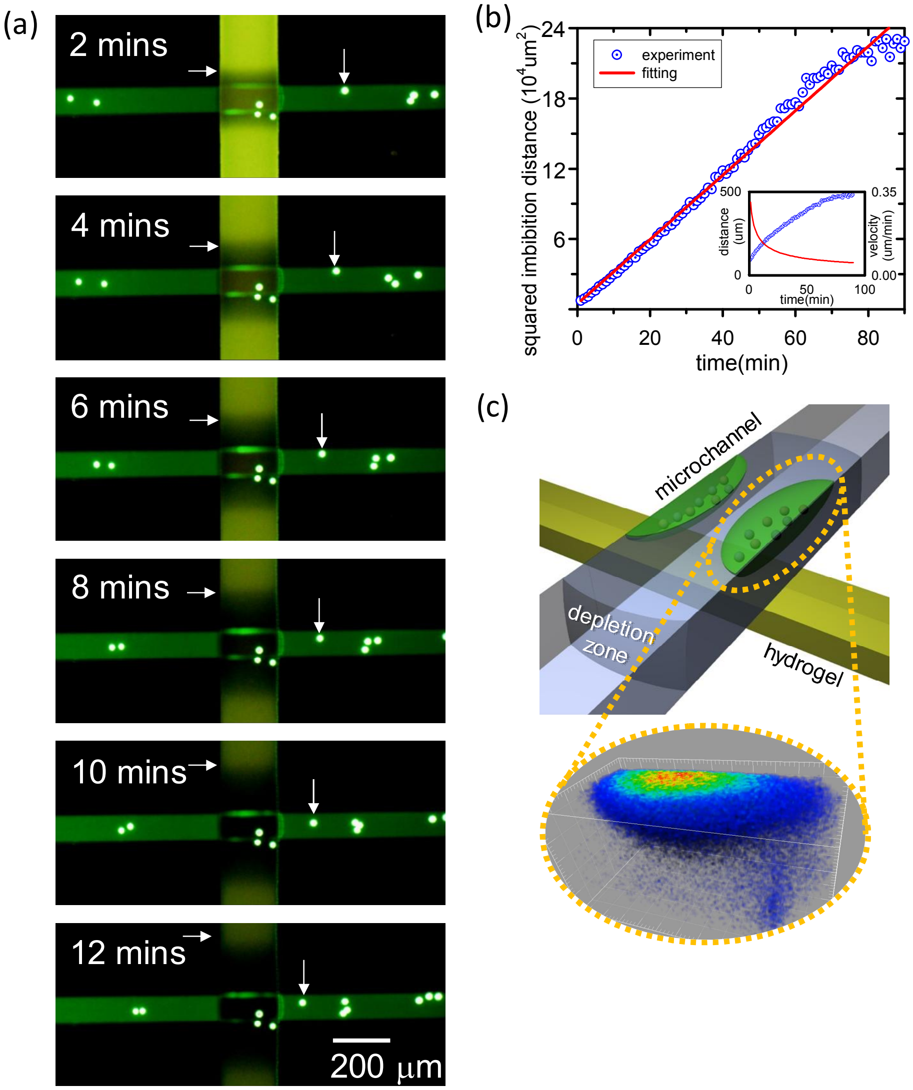

Figure 2.3 The formation of CICP zone. (a) The snapshots of a fluid flow driven by nanoporous hydrogel (see Supplementary Video 1) and (b) the plot of measured imbibition lengths as a function of time. The imbibition velocity is also plotted in the inset. (c) The confocal microscopic image of accumulating fluorescent dyes at the top corner of microchannel, confirming the formation of an ion-depletion zone at the bottom of microchannel.

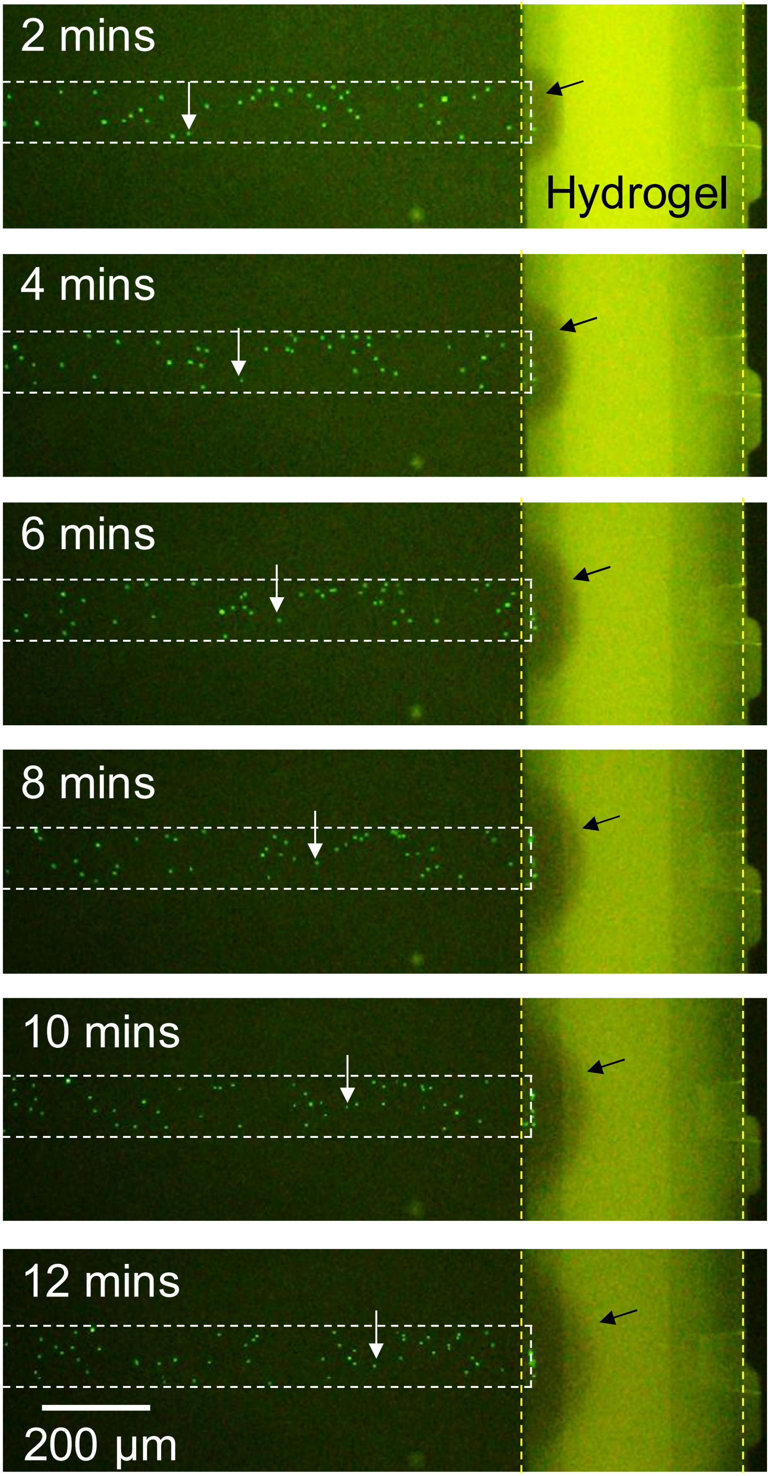

Figure 2.4 The snapshots of the microparticle movements toward the ionic hydrogel.

Furthermore, the dynamic measurements of the imbibition length revealed that it grew like a square root of time as shown in Figure 2.3 (b). This result was consistent with the classical Washburn’s equation that describes the temporal evolution of the imbibition length in a porous medium[45]. Thus, the imbibition rate shown in the inset of Figure 2.3 (b) indicated that the capability of absorbing solution decreased as a function of time. This fact significantly affected on CICP phenomenon as a restoration phase and would be discussed later on as well.

2.3.2 The measurement of hydrogel swelling

A hydrogel is known to have significant swelling property in the case of contacting water molecule. However, in order to focus on the capillarity as the only driving force of the perm-selective ion transportation, we would like to suppress the swelling using a confinement within the microchannel network. The free energy of osmo-poro-elasticity plays a key role to swell the hydrogel[42], but it was reported that the swelling could be suppressed by an external mechanical constraint such as a confinement within a microchannel[43, 44]. As shown in Figure 2.5, microscopic images of hydrogel ((a)~(d) within a confinement by a microchannel and (e)~(h) without the confinement) are captured at initial and after swelling. The volume of hydrogel is expanded less than 10% with the confinement (the volume expanded from 1mm × 400 μm × 50 μm to 1mm × 406 μm × 54 μm) and 77% without the confinement (the volume expanded from π (1385 μm)^2 × 1984 μm to π (1749 μm)2 × 2213 μm). Based on this measurement, the osmo-poro-elastic effect is successfully suppressed in this work.

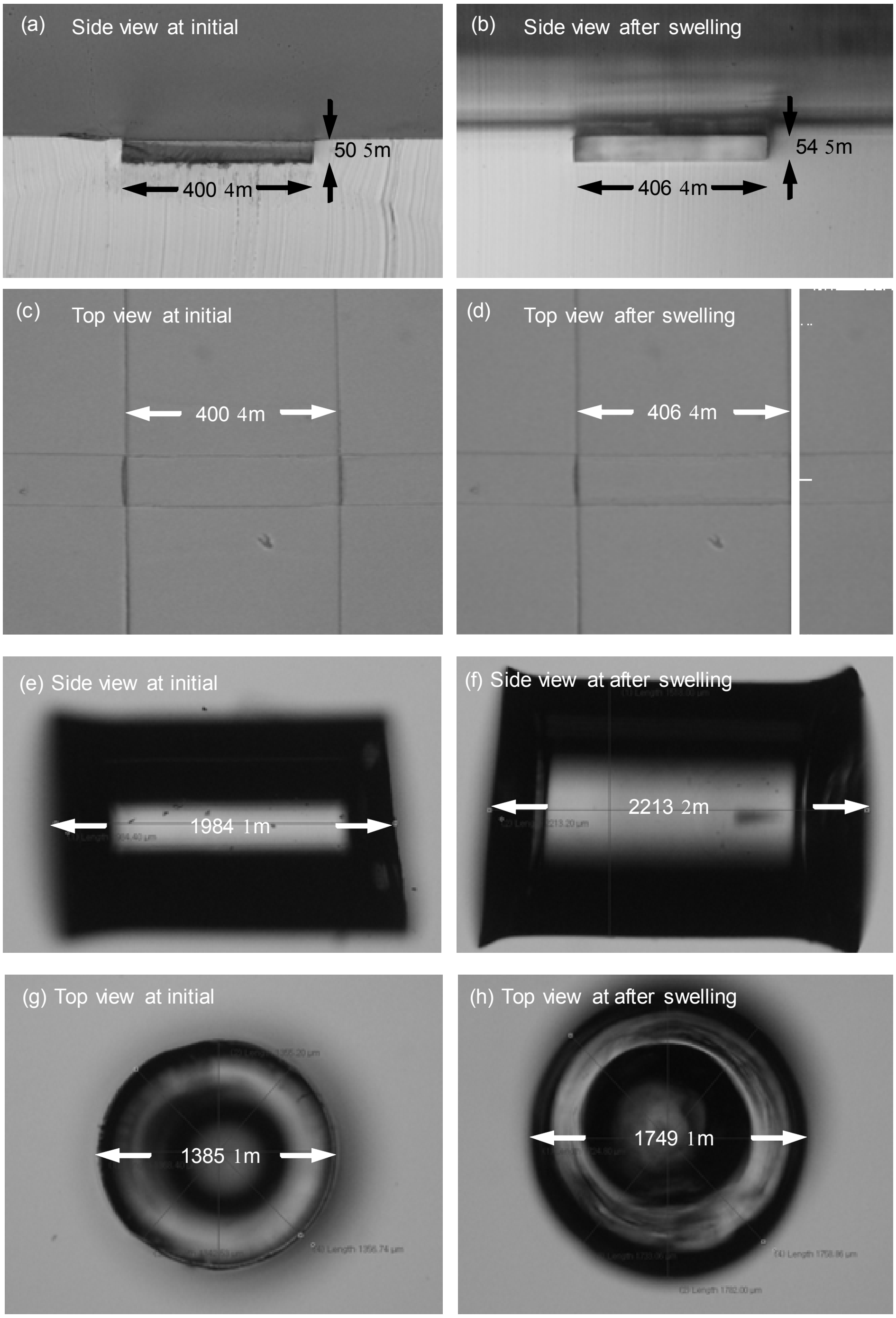

Figure 2.5 The microscopic images of the hydrogel before and after swelling. The hydrogel swelled (a) ~ (d) with a mechanical confinement within a microchannel and (e) ~ (h) freely without a mechanical confinement.

2.3.3 The formation of an ion depletion zone by CICP phenomenon

The conventional ICP phenomenon generated under an external dc bias results in significant concentration gradients at anodic and cathodic sides of a perm-selective nanoporous membrane. Typical behavior is that the ion concentration becomes extremely low at anodic side (referred to as an ion depletion zone) and enriches at cathodic side (referred to as an ion enrichment zone) in the case of cation selective membrane. While the mechanism involves complex interactions of electric fields and electrokinetic flows[46-48], the eye-catching fact in terms of engineering applications is that ICP can play as an electrical filter. This virtual barrier rejects the entrance of charged species into the ion depletion zone, so that it can be utilized as a water desalination / purification mechanism[17, 49] and a biomolecular preconcentration mechanism[11, 37]. Instead of an electrical bias, one can achieve the same ICP phenomena if another driving force pushes or pulls an electrolyte solution into a perm-selective membrane. Therefore, the capillarity was employed in this work to initiate ICP phenomena. In this sense, the ion depletion zone should also be formed in CICP system, which we confirmed using confocal microscope as shown in Figure 2.3 (c). Since the driving force for a liquid flow due to a capillarity was much weaker than that due to an electrical bias in general, the depletion zone initially stayed on the ionic hydrogel for a few hours (while the zone quickly expands in a conventional ICP system within a few seconds). A noticeable observation was that the fluorescent trackers were trapped at the top corners of a microchannel as shown in Figure 2.3 (c). If there was no such ion depletion zone, the trackers should be accumulated at the bottom of the microchannel. In the meantime, the center of the fluorescent cloud exhibited the brightest signal, since the flow converges into the hydrogel. Therefore, the confocal images with the most of fluorescent signals gathered at the corners of the microchannel provided the strong evidences of CICP formation on the hydrogel pad.

Compared to the conventional ICP system, the formation of the ion depletion zone in CICP system took several hours since it relied only on the capillary force. The fluorescent microscopic images were captured as shown in Figure 2.6 (a) ~ 2.6 (c). Each snapshot was captured at different time as indicated in the caption when the depletion zone expanded in maximum. As shown in Figure 2.6 (a), the fluorescent signal linearly decreased from the bulk solution as indicated at the line profile along A-A'. This was because the CICP system was driven only by capillarity, while the conventional ICP system has a sudden drop and a flat concentration profile with fast electrokinetic vortices.[31, 32, 47] By comparing with the reference signal intensities, the electrolyte solution at the interface of hydrogel pad was expected to be desalted with approximately 80 % removal efficiency. Here, ions were assumed to behave similar to fluorescent dyes. At least, the length of the depletion zone for ions and dye molecules were the same. This was confirmed by additional numerical simulations and experimental demonstrations in Appendix A. Although Figure 2.6 (a) was conducted on the center-connection device, the depletion zone asymmetrically expanded (i.e. no depletion zone was formed on the right side of the hydrogel). This was caused by an unavoidable residual flow from the level difference between the reservoirs. Detailed discussion would be given later on. To avoid the unwanted residual flow, the end-connection device was tested as shown in Figure 2.6 (b) and 2.6 (c). The concentration profiles had a similar linear drop and the desalting efficiency expected to be around 90%, which is similar to that of absorbed liquid by mangrove[39]. By comparing Figure 2.6 (b) with Figure 2.6 (c), the duration of the depletion behavior largely depended on the composition of the hydrogel. Increasing the volume fraction of charged group (AA in this work) provided a longer duration of CICP zone.

In Figure 2.6 (a), the depletion zone propagated asymmetrically. An inevitable liquid level difference between each reservoir in the center-connection device

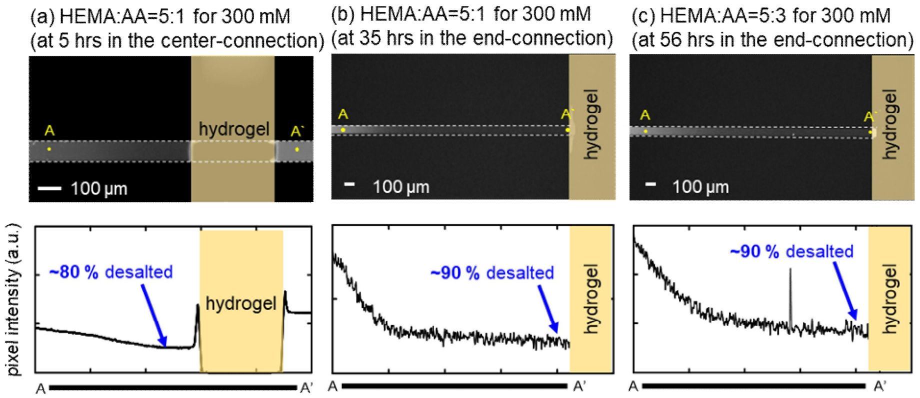

Figure 2.6 Spontaneous desalting by CICP. A fluorescent signal tracking through the microchannel with different compositions of the ionic hydrogel, (a) HEMA: AA = 5:1 in the center-connection device, (b) HEMA: AA = 5:1 and (c) HEMA: AA = 5:3 in the end-connection device.

resulted in a residual flow over hydrogel pad. In the case of the residual flow from right to left (with the imbibition flow still converging to the center from both reservoirs), the velocity of combined flow would increase at the right interface of the hydrogel and decrease at the left interface of the hydrogel. Based on the above theoretical analysis, low Pe would give a better depletion efficiency than high Pe. Since Pe is defined as a flow rate over a diffusion rate, there was a higher chance to have a stronger depletion zone at the left interface in Figure 2.6 (a) than the one at the right interface.

2.3.4 The restoration phase by a diminished imbibition

The aforementioned depletion zone was formed and sustained for a few hours, depending on the composition of the ionic hydrogel and the geometry of the microchannel. However, the ion depletion zone collapsed and the concentration restored to the bulk concentration as shown in Figure 2.7. This has never been observed in a conventional ICP phenomenon, since it continuously applied an external power. Note that the snapshots were captured every 1 hour, 7 hours and 8 hours in Figure 2.7 (a), 2.7 (b) and 2.7 (c), respectively. One interesting feature other than the appearance of the restoration phase was that the rate of the restoration phase was much slower than the rate of the depletion phase.

The transient analysis of CICP provided a clue for understanding the restoration phase. In CICP, the imbibition rate gradually decreases as a function of time as discussed above using the Washburn's equation[45]. Without the loss of generality, the imbibition rate was expressed as

$$u_{imb} = \sqrt{\frac{S}{4t}} \tag{4}$$

where u_{imb} is the imbibition velocity, S is the imbibition parameter, and t is the time. As shown above, u_{imb} as the source of CICP was proportional to $t^{-0.5}$, implying a high initial imbibition rate but it should decay with time.

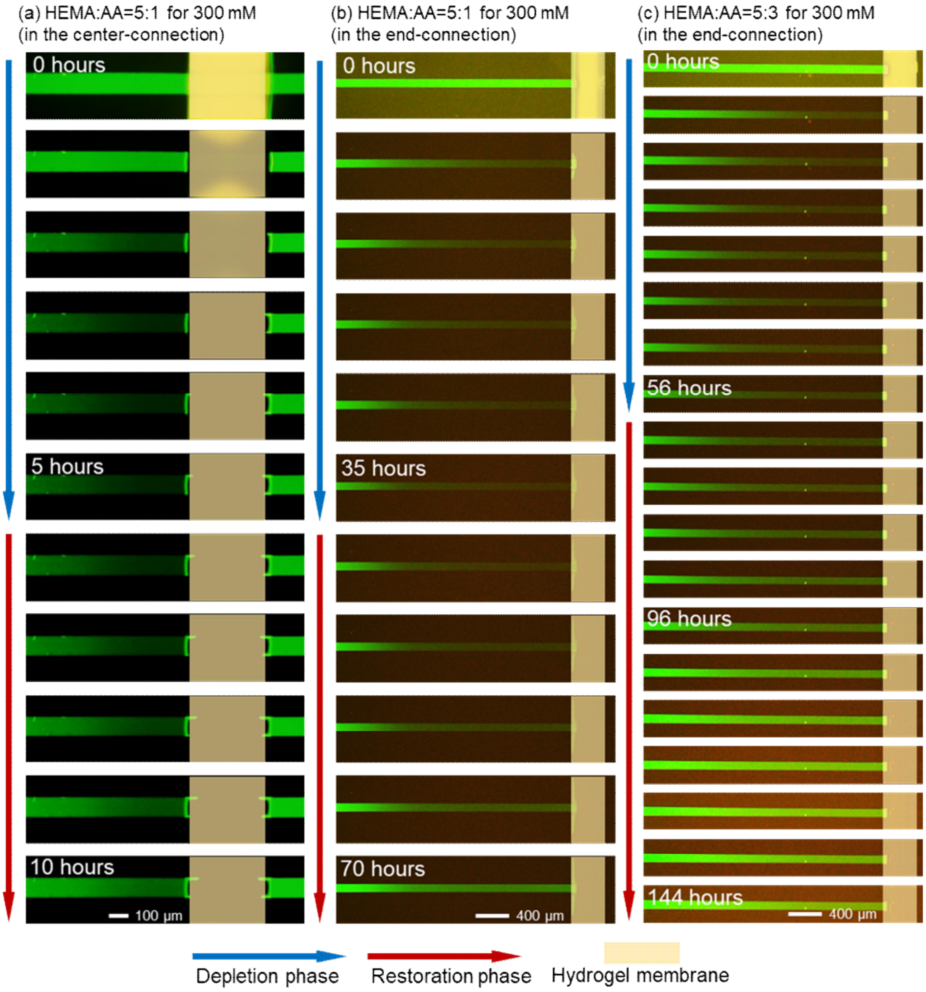

Figure 2.7 The depletion and the restoration phase of CICP. The dynamics of CICP system showing the transition from the depletion phase to the restoration phase with the different composition of the ionic hydrogel. (a) HEMA: AA = 5:1 in the center-connection device, (b) HEMA: AA = 5:1 and (c) HEMA: AA = 5:3 in the end-connection device..

2.3.5 Experimental analysis for the behavior of fluorescent dye

Typically, ionic fluorescent dyes such as sulforhodamine, Alexa, and Fluorescein have been used for visualizing the behavior of background electrolyte in microfluidics under assumption that the dye would behave with the electrolyte. However, the assumption could be concerned, because the dye would electrostatically interact with the cations and anions dissolved in the electrolyte.

we conduct additional experiments with various types of dyes and buffer concentrations. The properties of used samples are summarized in Table 2.1. In Figure 2.8 (a), KCl solution (#1) is driven to a cation selective hydrogel by the capillarity and the ion depletion zone is noteworthly generated. As the major cation (K^+) passes thorough the hydrogel membrane, the concentration of K^+ ion decreases near the membrane and the major anion (Cl^-) and the fluorescent tracker is also pushed away from the membrane because of the electrical neutrality. In Figure 2.8 (b), #2 has the same major anion with KCl solution but has larger cation than the pore size of the hydrogel. Thus, the cations of #2 (here we denote as TEA^+) is unable to pass through hydrogel so that all of ions (TEA^+, $Alexa^-$ and Cl^-) are accumulated near the hydrogel. By comparing Figure 2.8 (a) to Figure 2.8 (b), we conclude that smaller major cation size is demanded for the generation of the ion depletion region. In Figure 2.8 (c), DI + Alexa solution (#3) has the same cation with #2 and also shows the accumulation, leading to a conclusion that the larger major cation is expelled from the imbibition. In Figure 2.8 (d), Li-Alexa (#4) has small major cation (Li^+) and large major anion ($Alexa^-$). Li^+ passes through the hydrogel membrane and remaining anions should have been pushed away to satisfy the electrical neutrality. However, because of the large size of anion, all ions of Li^- Alexa solution are accumulated near the hydrogel. Comparing Figure 2.8 (a) to Figure 2.8 (c) and 2.8 (d), we conclude that small major anion size is also required for the generation of the ion depletion region. Lastly, Figure 2.8 (e) demonstrates

no.	**Electrolyte**	**Major cation**	**Major anion**	**Fluorescent tracker**	**Size comparison**
#1	DI + KCl 300 mM + Alexa 1 uM	K$^+$	Cl$^-$	Alexa$^-$	Li$^+$, K$^+$, Cl$^-$ << TEA$^+$, Alexa$^-$
#2	DI + TEA hydrochloride 3 mM + Alexa 1 uM	TEA$^+$	Cl$^-$	Alexa$^-$	
#3	DI + Alexa 1 uM	TEA$^+$	Alexa$^-$	Alexa$^-$	
#4	DI + Li-Alexa 1 uM	Li$^+$	Alexa$^-$	Alexa$^-$	
#5	DI + LiCl 300 mM + Alexa 1 uM	Li$^+$	Cl$^-$	Alexa$^-$	

Table 2.1 The electrolytes used for the tests. For simplicity, the cation and the anion of Alexa 488 are denoted as TEA+ and Alexa-, respectively. TEA is triethylamine. Depending on a relative concentration, major cation and major anion are selected as shown. #1 and #2 have the same anion and #2 and #3 have the same cation. #4 and #5 are added for confirming that both conditions (small size of major cation and major anion) should be satisfied to generate the ion depletion region.

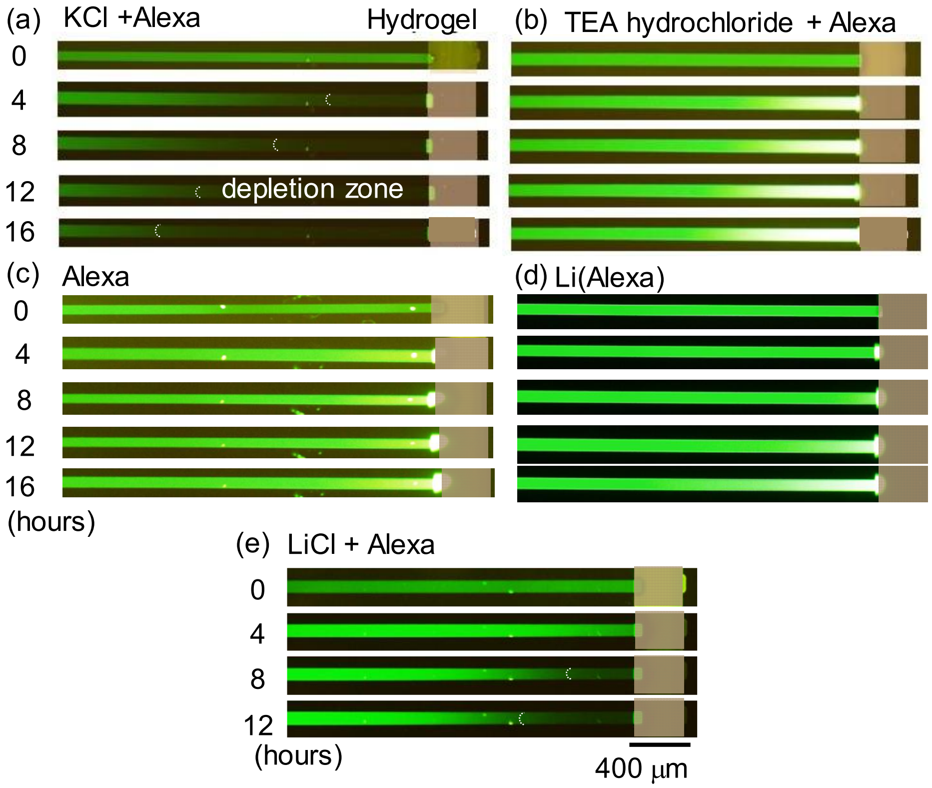

Figure 2.8 The electrolytes are (a) #1 (KCl), (b) #2 (TEA hydrochloride), (c) #3 (Alexa), (d) #4 (Li-Alexa) and (e) #5 (LiCl).

that the ion depletion zone is properly generated with 300 mM LiCl solution which has both small major anions and cations.

Here we consider five electrolytes and conclude that “both conditions” should be satisfied for the generation of the ion depletion zone. The small major co- and counter-ion size are necessary conditions to generate the ion depletion zone but if one of the condition is missing, both ions are accumulated near the hydrogel membrane showing the accumulation phase (Table 2.2).

Therefore, if one observed the ion depletion zone by tracking large fluorescent dye ions, this confirms that the small major counter-ions (here K^+) have penetrated through the hydrogel and the small major co-ions (here Cl^-) and fluorescent tracker are simultaneously pushed away from the hydrogel. Conclusively, in this work, the movement of dye molecule is able to infer the behavior of ions.

no.	Electrolyte	Counter-ion size	Co-ion size	CICP phenomena
#1	DI + KCl 300 mM + Alexa 1 uM	small	small	depletion
#2	DI + TEA hydrochloride 3 mM + Alexa 1 uM	large	small	accumulation
#3	DI + Alexa 1 uM	large	large	accumulation
#4	DI + Li-Alexa 1 uM	small	large	accumulation
#5	DI + LiCl 300 mM + Alexa 1 uM	small	small	depletion

Table 2.2 The conditions for the generation of ion depletion region in CICP system.

2.3.6 Asymmetric formation of the ion depletion zone in the center-connection device

While the depletion region is adequately developed at the left hand side in the Figure 2.6 (a), the fluorescent intensity that qualitatively represents an ion concentration remained unchanged at the right hand side. This unbalance mostly caused by an external residual flow, which is induced by an inevitable liquid level differences between two reservoirs. It is explained by the change of fluid flow caused by the external residual flow as shown in Figure 2.9.

The direction of residual flow ($u_{residual}$) is right to left, while the imbibition flow (u_{imb}) symmetrically converges into the hydrogel. The combined flow (u_{total}), thus, results in high Pe on the right hand side. Through the analytical solution, the depletion region would be destroyed at the right hand side and maintains at the left hand side due to the lower Pe. In addition, the residual flow also affects to the duration time of depletion region. The residual flow carries ions from right to left so that the depletion region is replenished by the ions, leading to the short duration of the depletion zone in case of this center-connection device. This result is confirmed in Figure 2.7.

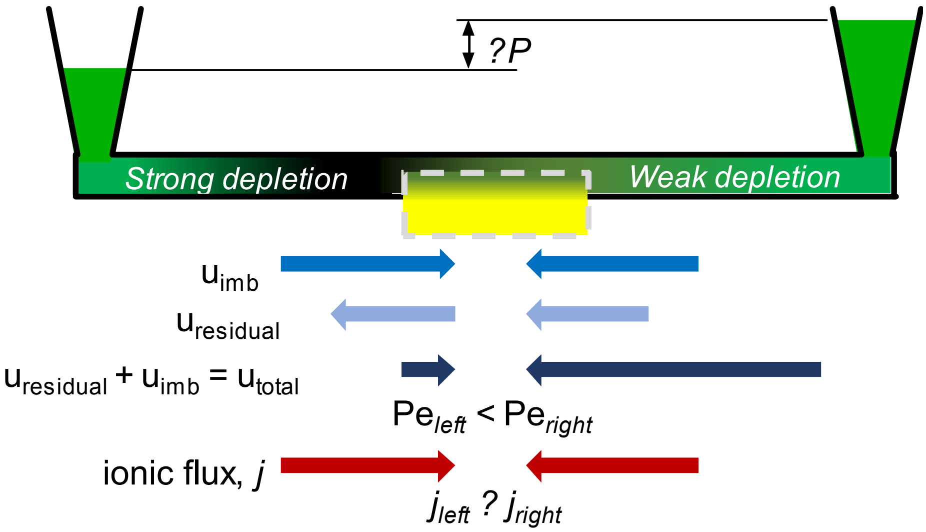

Figure 2.9 The schematic diagram of total fluid flow under the consideration of an external residual flow by the level difference between reservoirs.

2.4 Conclusions

In this study, we proposed a new ion concentration polarization phenomenon driven by capillarity. Instead of an external electric field, the inherent capillarity of nanoporous network drove a perm-selective ion transportation through the network, leading to the ion depletion zone near the ionic hydrogel. While state-of-the-art desalination method utilizing a size exclusion, a thermal or electrical energy have remarkably advanced, the high level of energy requirements have hampered to develop a small-scale desalination / purification system. The fact that the CICP mechanism was working without any electrical power source offered significant merits in terms of the power consumption and the stable operation compared to the conventional electrokinetic ICP mechanism and other state-of-the-art large scale desalination methods. Therefore, the present spontaneous desalting mechanism can lead to a power free desalination system that is significantly useful in a remote/rural and a disaster-stricken area. In order to achieve such a system, maintaining a quiescent fluid near the nanoporous membrane (i.e. low Péclet number), enhancing the intrinsic surface charge of the membrane (i.e. high ionic flux) and sustaining an imbibition at a certain level (i.e. preventing restoration phase) are strongly required.

Chapter 3. Bio-based Membranes for Nanofluidic Applications

3.1 Introduction

Since last two decades, nanofluidics has been drawn significant attentions due to its new physics and various applications that have never been demonstrated by microfluidics[50, 51]. Such advances were originated from unique surface effect of surface charge[52, 53] electrical double layer overlap[1, 54] or surface slippage[55, 56] etc. Those unique phenomena were extensively applied for novel engineering applications in the field of bio-/chemical-analysis[57, 58] environmental science[19] and lab on a chip application[59], etc., showing superior performance compared to the microfluidic applications. To achieve these nanofluidic properties, nanofabrication techniques were essential to be developed. In early stage of nanofabrication, sophisticated and expensive methods in high class cleanroom should be utilized. Focused Ion Beam (FIB) and Nano Imprint Lithography (NIL) were the representative examples of such nanofabrication. In FIB (or E-beam) lithography, a focused beam of ions (or electrons) is employed to create a fine nanometer-scale structure by expensive beam-writing equipment in high class cleanroom. NIL is relatively simple and cheap fabrication method using nanostructured mold, but it still requires the pre-fabrication of exquisite and robust nanostructured mold.

When trying to enhance the nanofluidic effect, nano-porous-medium which has intrinsic nanostructure (eg. graphene oxide[60, 61], ionic hydrogel[10, 62], polymeric resin[3, 12, 63], self-assembled nanoparticles[64, 65] etc.) could be also utilized. Porous medium based nanofabrications are not only cheap but also scalable so that they have been applied in various applications that may need high-throughput requirement[66]. Dielectric breakdown of the PDMS substrate is also used as a nanojunction[67, 68]. When the highly focused electric field was induced between PDMS based microchannels, trapezoidal nanojunction was created.

Such endeavors finally reached to the low cost and disposable application, particularly useful for point-of-care device in remote settings. Biocompatible materials were actively employed for the building block in such device. For example, most of micro/nanofluidic functions were rebuilt with paper-based microfluidics recently[69-71]. Hydraulic pumping in conventional microfluidic system was appropriately replaced by capillary force of the cellulose fiber[72]. For the visualization of the biological / chemical reaction, colorimetric assay was implanted on paper-based microfluidics. Biomolecule preconcentrator[73] and separator[74] or energy harvesting system[75] with permselective membrane were also demonstrated by paper-based micro/nanofluidic device. However, the choice of materials for the nanostructure is still limited within non-biocompatible material, while few biocompatible materials were demonstrated with sophisticated treatments such as epoxy filling in wood-based nanostructure[76] and effective reduction of phytochemicals[77, 78]. In the light of such need, new biocompatible and biodegradable materials originated from living organisms were demonstrated as a nanoporous membrane in this work. Human nail were proven to be a proper candidate for the nanofluidic functionality. The formation of ion depletion zone, limiting and overlimiting current behavior and surface-governed conductance were experimentally investigated. Simple but essential demonstrations in this work would have a great potential to be developed as full-biodegradable and eco-friendly nanofluidic platforms.

3.2 Nail plate as a perm-selective membrane

Human nail plate was selected as a perm-selective membrane because several literatures referred that the human nail is composed of disulfide-linked keratinous tissue which is negatively charged[79] and allows the interesting mass transport as shown in Figure 3.1 [80]. Nail was gradually hydrated, meaning that human nail is the porous medium[81] and a number of studies showed that various ions and biological molecules could pass through the nail plate by diffusion or electro-diffusion as shown in Figure 3.1 (b) and Figure 3.1 (c)[82, 83]. In addition, pore structure was observed in SEM image in Figure 3.1 (d). bottom view SEM image of the nail plate showed that the nail plates have a nanopore. There were several literatures to support that ion transport in human nail plate highly depended on its physicochemical properties such as porosity, pore size, and surface charge[84]. For example, effective pore size of the nail plates has been estimated to be around 0.7 nm[85]. These evidences suggest that pore structure in the human nail is nanoscale and has nano-electrokinetic properties that affects to ion transport inside the human nail.

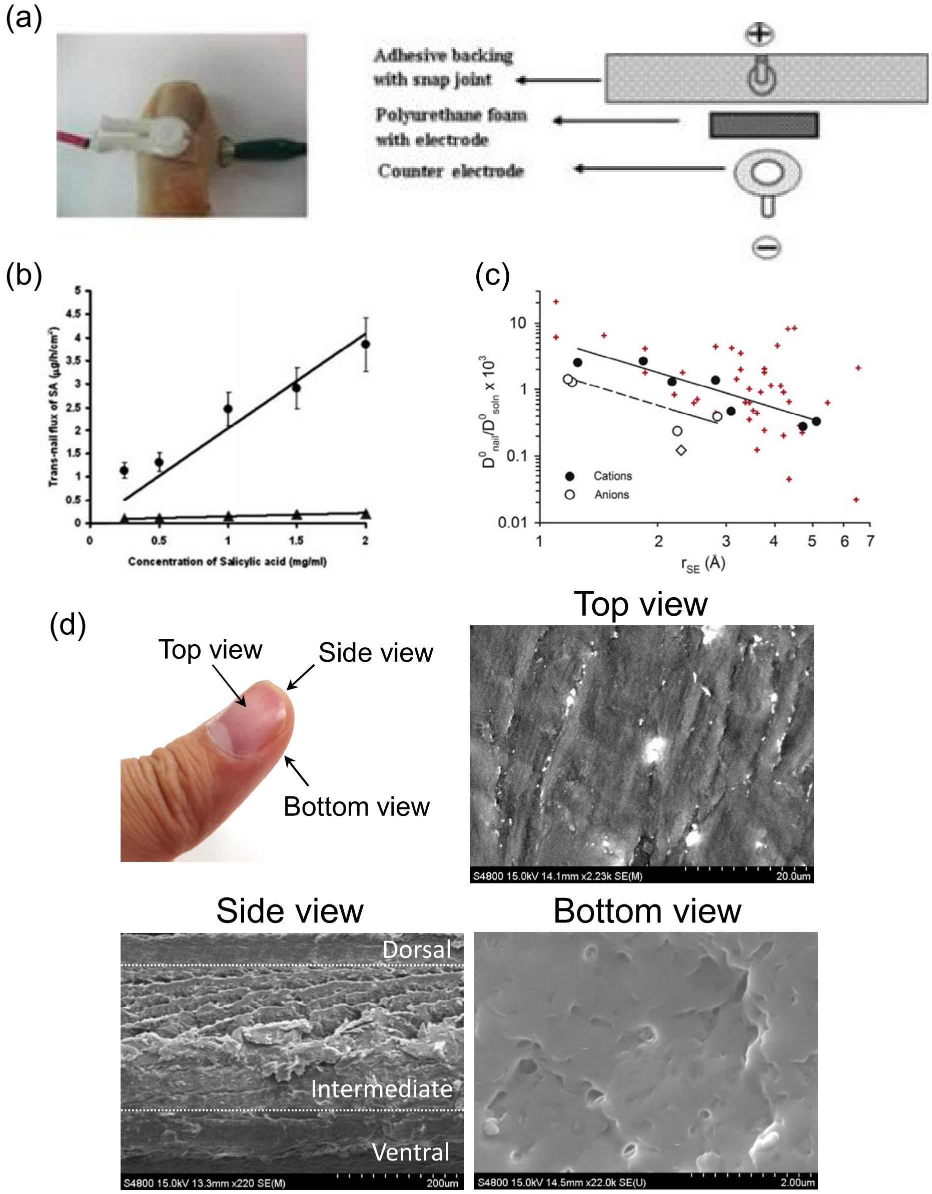

Figure 3.1 (a) iontophoretic mass transport of the nail [80] (b) Trans□nail flux of salicylic acid at different concentrations of SA. The filled triangles represent the passive transport and the filled circles represent iontophoretic transport. [82] (c) Double logarithmic plot of the effective diffusivity of ions in the nail plate relative to their diffusivity in solution plotted versus Stokes–Einstein radius, r_{SE}.[83] (d) SEM image of the human nail plate

3.3 Materials and methods

3.3.1 Nail device fabrication

Fabrication of the device using human nail (named as “nail device”) as a nanoporous membrane for visualization of ICP phenomenon and I-V characteristic measurement was as follows. The main building block of the device was PDMS (Sylgard 184 silicone elastomer kit, Dow Corning, USA). PDMS base was mixed with a PDMS curing agent at 10:1 ratio and degassed in a vacuum chamber for one hour. The mixture was poured on the petri dish until the depth of mixture was 0.5 cm and was cured on the oven for four hours at 75 °C. The cured PDMS was detached from the petri dish and cut into two blocks which had the dimension of 5 cm (width) × 5 cm (height) × 0.5 cm (depth). The center of each block was punched by biopsy punch (BF-15F, Kai Medical, Japan) to create the hole (diameter: 1.5 mm) which was used as the channel of the device. The nail plate was prepared with dimension of 2 mm (width) × 2 mm (height). The thickness of the nail plate was 0.9 mm. As shown in the Figure 3.2 (a), nail plate was sandwiched between two PDMS blocks and then they were irreversibly bonded with oxygen plasma (CUTE-MP, Femto Science, Korea) treatment. Top side and the bottom side of the bonded device was cut to secure the focal length of optical microscope for clear observation of the channel. The pipette tips as reservoirs were inserted to the hole of the PDMS block. Assembled device was shown in Figure 3.2 (b).

For conductance measurement of nail plate, nail plate was cut to dimension of 13 mm (width) × 4.5 mm (height) and the depth of the nail plate was 0.9 mm. Nail plate was immersed in the 9 mL DI water for 24 hours to hydrate it. After that, it was immersed in the 9 mL KCl solution at a concentration ranging from 0.01 mM to 100 mM for 24 hours as shown in Figure 3.3. The nail plate was taken out and wiped off. Crocodile clip was connected both end of the nail plate and the voltage was applied stepwise from -10 V to 10 V at 2 V/sec. The current values at each step were recorded by customized Labview program. The conductance values were calculated from the slope of the I-V curve.

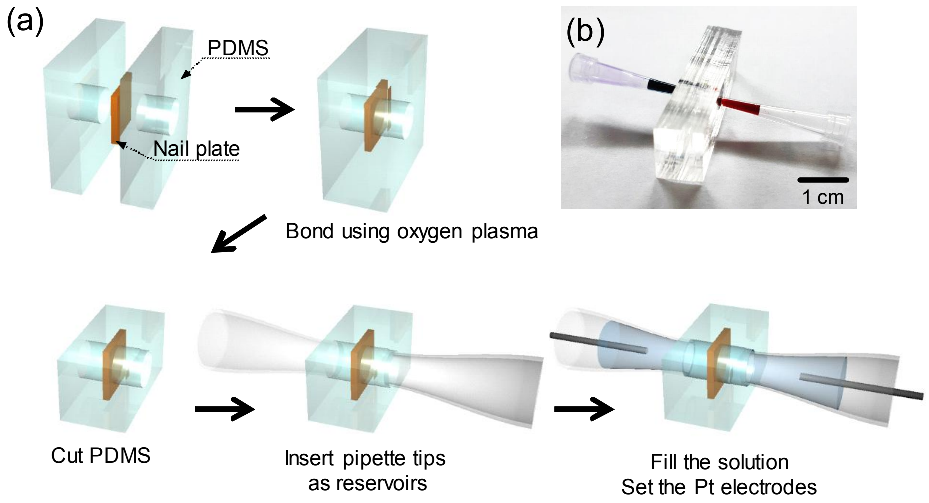

Figure 3.2 The fabrication process of the nail device. (b) The photo of assembled nail device

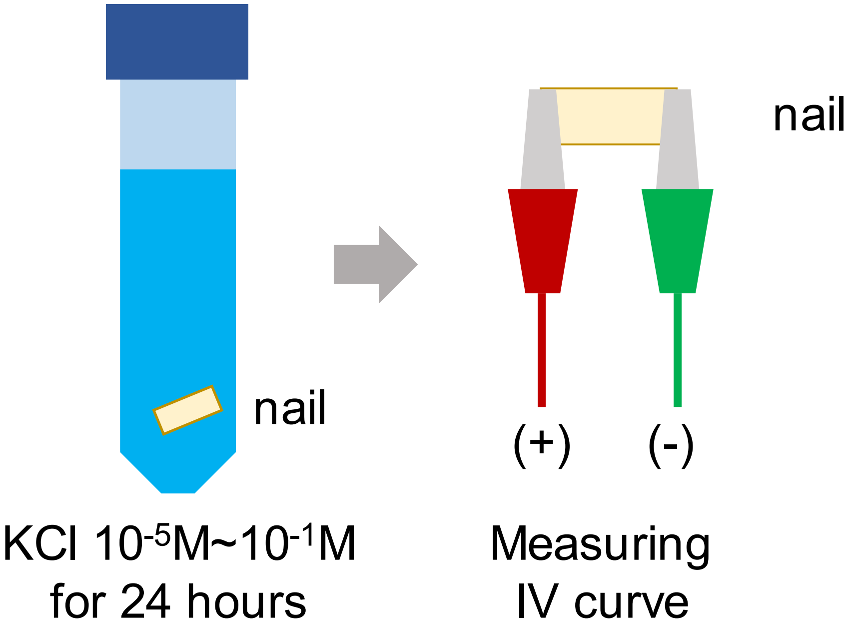

Figure 3.3 schematic diagram of the conductance measurement experimental process of the nail plate

3.3.2 Experimental setup

For visualization experiments for the nail device, PBS solution (0.001X) with Alexa 488 fluorescent dye (1 μM) was used for electrolyte. After injecting the electrolyte solution on the device, wait at least 2 hours so that the nail plate was sufficiently wetted with the solution48. 100 V of DC bias was applied to the device by a source measure unit (Keithley 238, USA) via Pt electrodes at the reservoirs. The propagation of ICP layer were captured by an inverted fluorescent microscope (IX53, Olympus) and CellSens program.

For the I-V characteristic measurement of the nail device, PBS solution (0.001X) was used for electrolyte as well. The voltage was swept from 0 V to 100 V at 1 V/min. The current values at each step were recorded by customized Labview program.

3.4 Results and discussion

3.4.1 The formation of ion depletion zone upon nail device

When DC bias is applied on a permselective nanoporous membrane which is immersed in an electrolyte solution, significant concentration gradient occurs near the membrane[86]. An electric field induces the asymmetric ionic flux inside the permselective membrane, causing ion concentration imbalance. Typical behavior of ions with the cation-selective membrane is that ions were depleted at anodic side (i.e. ion depletion zone) and were enriched at cathodic side (i.e. enrichment zone) of the membrane[24, 32]. This phenomenon is called ICP phenomenon[17, 46]. In other words, the presence of the ICP phenomenon (or appearance of ion depletion zone at anodic side) near the membrane is the key evidence that the membrane is nanoporous.

As shown in Figure 3.4 (a), negatively charged fluorescent dye (Alexa 488) was depleted at the anodic side with 100 V DC bias in nail device. The concentration of fluorescent dye (1 μM) inside the solution were sufficiently low compared to that of major carriers (PBS 0.001X) so that the fluorescent dye rarely disturbed the device and it just used for tracer of the major carrier[87]. Therefore, the depletion region of the fluorescent dye represented the existence of ion concentration gradient near the anodic side of the nail plate, which means that the human nail is not only a medium of mass transfer but also has the permselectivity. Also, the enrichment region was developed at the cathodic side. These facts strongly supported that a nail plate can be utilized as a cation-selective membrane.

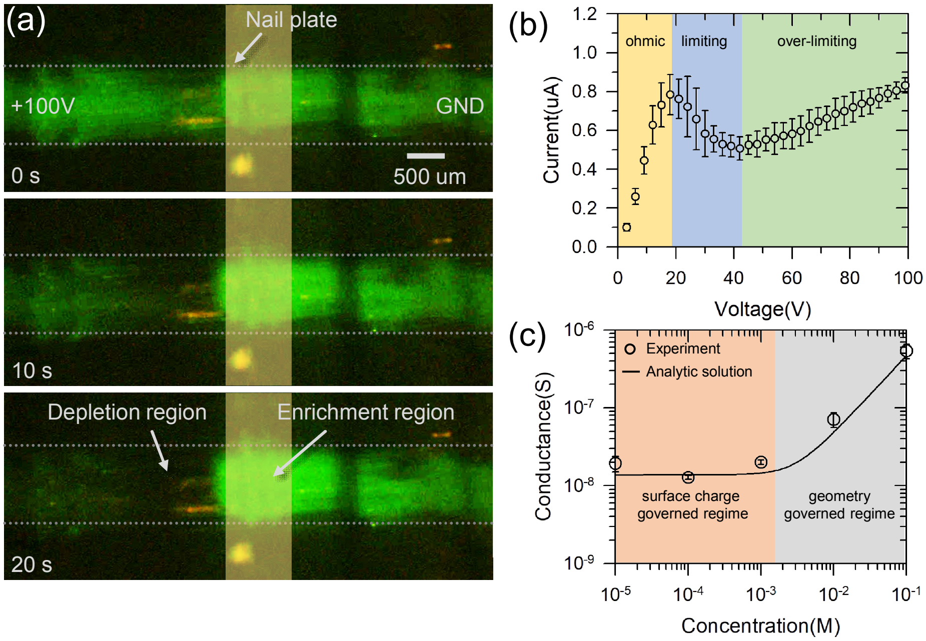

Figure 3.4 (a) The visualization of an ion depletion zone and an ion enrichment zone resulted from ICP phenomenon using nail device. (b) I-V characteristics of nail device. (c) Conductance profile of the nail device.

3.4.2 The I-V characteristics of the nail device

I-V characteristics in Figure 3.4 (b) showed typical linear sweep voltammetry of micro/nanofluidic device which associated with a permselectivity. Without a permselective membrane, I-V characteristic of the device shows only linear ohmic response. However, I-V characteristics are divided in three distinct regions with a permselective membrane; Ohmic, limiting and overlimiting[32, 54, 88, 89]. In the ohmic region between 0 V and 20 V, current increases linearly as a function of voltage as shown in Figure 3.4 (b) because the device has constant conductance until ICP is initiated. The following region is called the limiting region. In theory, the development of the ion depletion region near the anodic side of the membrane leads the decrease of conductance of the device so that current value would be saturated. In realistic conditions (the sweep rate was not slow enough), a peak current was appeared before saturation[90, 91] called overshoot effect. As shown in Figure 3.4 (b), a peak current was observed around 20V, and after that, constant current region (limiting current region) followed very shortly. As the voltage increased further, the overlimmiting region appeared. In overlimiting region, current value increased with the increasing voltage because of the electrokinetic reasons such as surface conduction[30, 31, 92], electroosmotic convection[32, 47] and electroosmotic instability[33, 88] as shown in the Figure 3.4 (b). These I-V characteristics is a fingerprint that the nail plate is a permselective nanoporous membrane. In many previous studies, overlimiting current appeared less than 10V in conventional perm-selective media such as Nafion [91, 93], but the overlimiting current appeared in 40V in nail plate as a permselective membrane. The reason is that the nail plate has much lower surface charge and Donnan concentration than conventional permselective media such as Nafion. Thus, the low perm-selectivity of the nail plate allows it to reach overlimting current at high voltage.

3.4.3 The conductance profile of the nail plate

The conductance curve in the micro/nanofluidic device as a function of electrolyte concentration differs from the behavior of the typical mesoporous membrane device. In the case of the mesoporous membrane, the conductance through the membrane is linearly proportional to the concentration of the bulk electrolyte solution because the concentration inside the membrane become equal to the concentration of electrolyte solution outside the membrane. However, in the case of the permselective nanoporous membrane, the conductance through the membrane formed a plateau below a threshold electrolyte concentration4 called "surface charge governed regime." This constant conductance region reflects that surface charge of the membrane affects the ion concentration inside the membrane at a low electrolyte concentration. In the meantime, the conductance turns to a linear profile beyond the threshold concentration called "geometry governed regime." As shown in Figure 3.4 (c), the nail plate should be a permselective membrane since the behavior of nail plate conductance followed the behavior of permselective nanoporous membrane conductance. See supporting information for the fabrication and measurement method of nail device.

The value of surface charge of the human nail can be obtained from this conductance profile because the surface charge relates to the conductance of the membrane. The conductance of the membrane (G_{mem}) was theoretically calculated as64

$$G_{mem} = \alpha\left[\mu_+\left(\sqrt{4c_0^2 + N_w^2} + N_w\right) + \mu_-\left(\sqrt{4c_0^2 + N_w^2} - N_w\right)\right] \qquad (5)$$

where α is empirical coefficient, μ_+ and μ_- are the electrophoretic mobility of cation and anion, respectively, c_0 is the bulk electrolyte concentration and N_w is the surface charge concentration (i.e. Donnan concentration) which is defined as

$$N_w = -\frac{2q_s}{Fa} \tag{6}$$

where q_s is the surface charge density, F is the Faraday constant and a is the equivalent hydrodynamic radius of the nanopores inside the membrane[94]. Here equivalent hydrodynamic radius a of nail plate is 0.7 nm[85]. α and Nw were obtained from fitting curve of the conductance profile. In this case, α was estimated by 1.5×10^{-2} C·m/mol and Nw was estimated by 6 mM. From these values, the surface charge of the nail plate was estimated by -0.2 mC/m^2 and it fits well with literature value (~0.1 mC/m^2)[85]. While this value was lower than the surface charge of silicon (-15 mC/m^2) and Nafion membrane (~ -200 mC/m^2)[3], it still has a permselectivity, and therefore, the nail plate was proven to be used for permselective membrane again. These conductance values and Donnan concentrations were organized in Table 3.1. The conductance value and Donnan concentration of hen egg yolk and albumen was descripted at the Appendix B.

	nail	**albumen**	**yolk**	**Nafion**	**silicon nanochannel**
$\lvert q_s \rvert$ (mC/m^2)	0.26 ± 0.08	60.1 ± 12.3	46.3 ± 8.7	~200	~15
N_w (mM)	7.75 ± 2.25	41.5 ± 8.5	16.0 ± 3.0	~720	depending on geometry

Table 3.1 Comparisons of surface charge and Donnan concentration of nail plate, egg yolk and albumen with other materials

3.5 Conclusions

Most of the conventional nanostructures in a micro/nanofluidic applications are non-biocompatible and fabricated by sophisticated equipment in high class cleanroom facilities. On the other hands, biocompatible materials such as paper or woven thread in microfluidic applications were recently reported. Because of this gap, novel fabrication using a functional and biodegradable materials should be required to design a low-cost and eco-friendly micro/nanofluidic applications. In this work, human nail plate and denatured hen egg yolk/albumen as a functional biomaterial were introduced as a permselective nanoporous membrane. These materials were originated from the living organisms unlike most of the previously reported nanoporous materials. Permselectivity of these membranes was verified by ICP phenomenon. Surface charge density of these membranes was obtained by conductance profile. Compared to the sophisticated nanostructures, the presenting materials showed relatively low repeatability. This is inevitable because of the variety of nail plate. The device should be carefully sealed for improving the repeatability. Although nail device have these limitations such as low surface change and low repeatability, it have great potential for fully biodegradable low-cost micro/nanofluidic devices for point-of-care disposable devices in remote settings.

Chapter 4. Undulated Nafion Membrane For Investigation of Electroconvective Instability

4.1 Introduction

In the fluidic system involving permselective membrane such as fuel cell, electrodialysis, capacitive deionization and micro/nanofluidic platform, electrical power efficiency is one of the important issues since the existence of limiting current means that the system has the nonlinear I-V characteristics. The depletion region near the permselective membrane increase the electric resistance of the system and limiting current appear. However, in realistic conditions, overlimiting current which means that the current increases again has been observed [22, 30, 32, 38, 95]. Therefore, many researchers have studied about the overlimiting regime that can increase the electric power efficiency. Dydeck *et al.*[30] theoretically classified the origin of the overlimiting current depending on the characteristic length scale ; Surface conduction (<~*O*(1) μm)) , electroosmotic flow (~*O*(10) μm) and electroosmotic instability(>~*O*(100) μm)). Since the most of the electrokinetic platforms are in electroosmotic instability regime, researchers such as Rubinstein and Duckhin assumed that the system was in electroosmotic instability regime and showed that the electroconvection is one of the cause of electroosmotic instability. It is known that electrocoevction near the permselective membrane can be expressed by two mechanisms: Rubinstein's mode and Dukhin's mode. As shown in the Figure 4.1 (a), small perturbation of the space charge layer generates tangential electric field and it cause the electroconvection in Rubinstein's mode. In contrast, the protruding structure of the surface of membrane generates tangential electric field and it cause the electroconvection in Dukhin's mode as shown

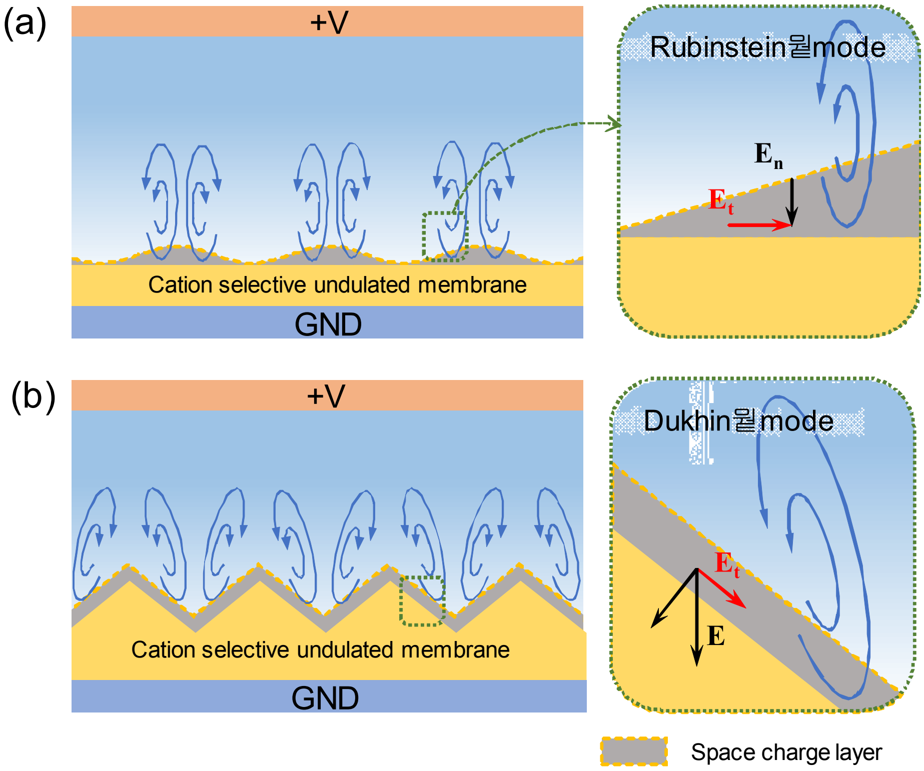

Figure 4.1 schematic image of electroconvection near the perm-selective membrane, (a) Rubinstein's mode and (b) Duckhin's mode

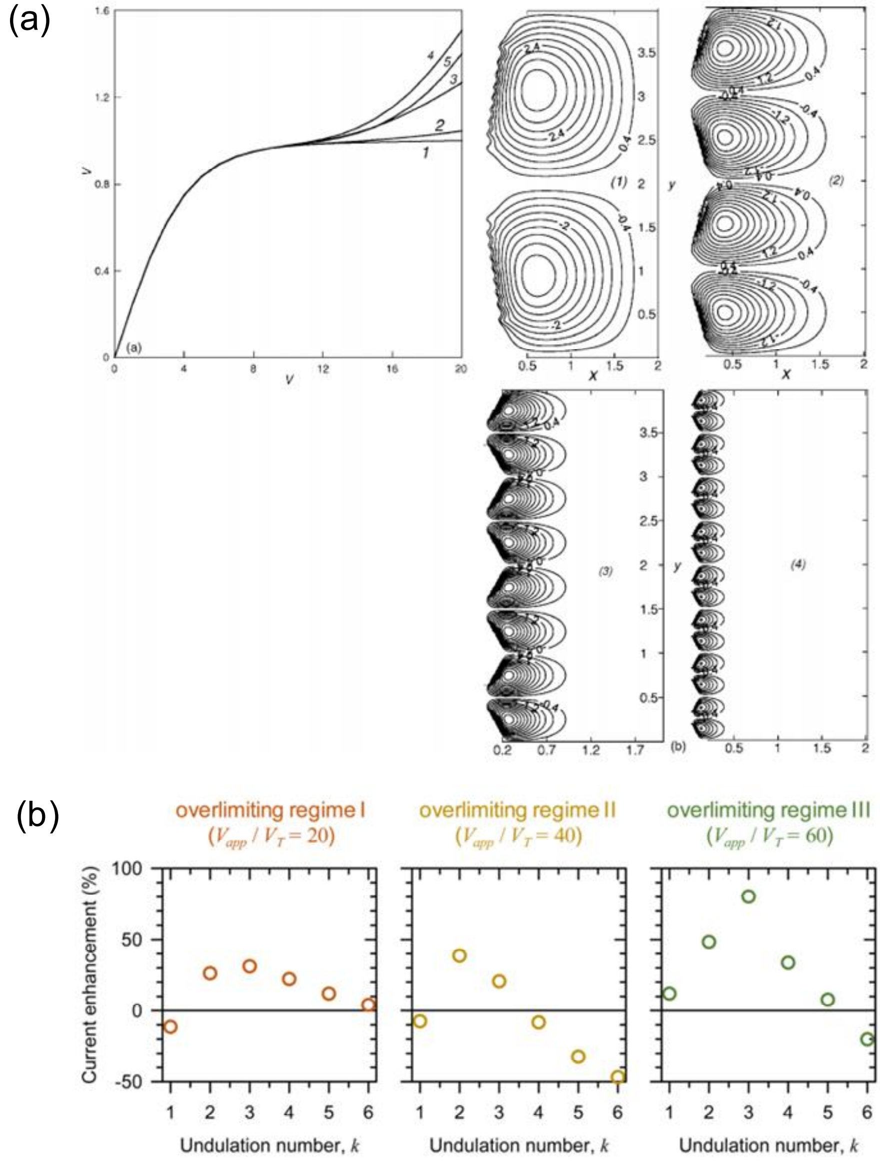

Figure 4.2 (a) numerical simulation of I-V characteristics (1, unperturbed surface k= 0; 2, k= 1; 3, k= 2; 4, k= 4; 5, k= 8) of undulated surface system and electroconvective vortices near the permselective undulated surface. (1, k= 1; 2, k= 2; 3, k= 4; 4, k= 8) [34] (b) Numerical simulation of enhancement of the overlimiting current in three regime, overlimiting regime I, II, III [96]

in Figure 4.1 (b) [96]. In realistic condition, Rubinstein's mode and Dukhin's mode are expected to compete to generate electroconvection in groovy surface of membrane. In the case of device which has high characteristic length scale (the electroosmotic instability regime), several studies have showed that the electroconvective vortices near the undulated surface mixed concentration and enhanced the overlimiting current.[34, 96] As shown in Figure 4.2 (a) and (b), overlimiting current was enhanced depending on the wave number, *k.* interestingly, enhancement of overlimiting current had peak point depending on the wave number, *k*.

In this work, micro scale of undulated permselective membrane surface was fabricated and tested to enhance the electroconvection in Dukhin's mode. In particular, we visualized electroconvective vortices and compared the I-V characteristics in two characteristic length scale; 15 μm and 150 μm.

4.2 Materials and methods

4.2.1 Undulation device fabrication

Detailed fabrication process of top PDMS from the figure 4.3 was as follows. Firstly, (i) commercial tape(Scotch magic tape, 3M, USA) was attached to the portion other than the experimental domain in order to ensure that the plasma treatment was treated only at the desired portion. Then plasma treatment was treated about 6 seconds. After that, (ii) detach the tape and Nafion was coated at 4000 rpm, 30 seconds by using spin coater. Then the (iii) tape was attached again to tear off the desired portion of Nafion. (iv) Undulation patterned Nafion was remained after detach the tape.

The fabrication of the device with undulated permselective surface to measureing the IV characteristics (named as “undulation device”) was as follows. The main building block of undulation device was PDMS material as schematically shown in Figure 4.3. The final device consist of two layer of PDMS blocks. Bottom was for patterned microchannel to inject microparticles and top was for microchannel to inject electrolyte solution as shown in Figure 4.4. However, the channel for the microparticles was not used because it was not necessary for the whole experiment so that the inlet of the channel was sealed. Silicon masters were prepared using SU8 photoresist for both bottom PDMS and top PDMS. Both bottom and top PDMS had same depth, 15 μm or 150 μm. The PDMS blocks were fabricated as follows. The PDMS material mixed with a curing agent at 10:1 ratio was poured on the silicon masters that had a desirable microchannel pattern. Then the polymer solution was cured in an oven for 4 hours at 75 ^{o}C. The top PDMS block that had undulated pattern and bottom PDMS block that had microchannel for injecting microparticles were irreversibly bonded by oxygen plasma treatment as shown in Figure 4.4. Undulated surface shape was isosceles right triangular

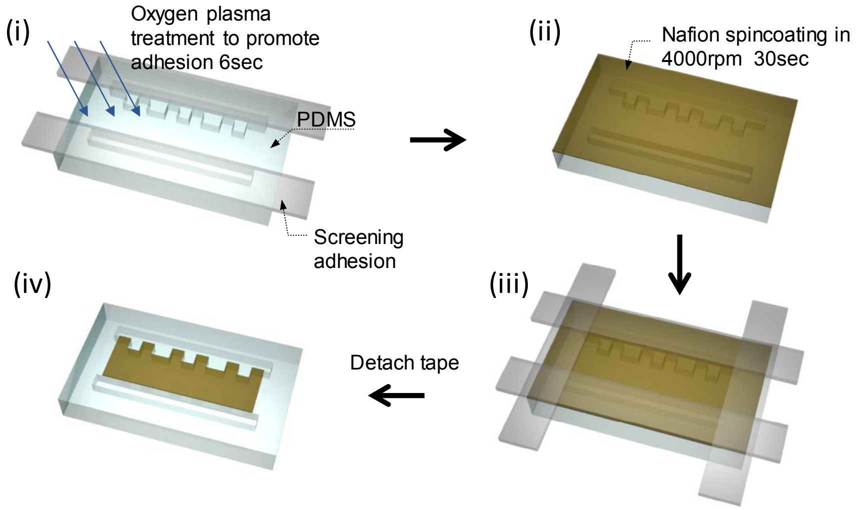

Figure 4.3 The Fabrication process of the undulation device

waves and the wave length of the undulation was L (50 μm, 100 μm, 200 μm, 500 μm).

For the visualization of the vortices, top PDMS which had sin wave undulated shape with amplitude 100 μm and wave length 200 μm.was irreversibly bonded with glass and Depth of the device was 150 μm

4.2.2 Experimental setup

For IV characteristic measurement of undulation device, KCl solution (1 mM) with Alexa 488 (1 μM) was used for electrolyte and electrical voltage was applied between “voltage inlet” and “GND inlet” as shown in Figure 4.4. The constant flow that had 0.5 μl/min flow rate applied on GND inlet and voltage inlet to confine the experimental domain. Cyclic voltammetry was applied from -50V to 50V, increasing by 1V every 20 seconds.

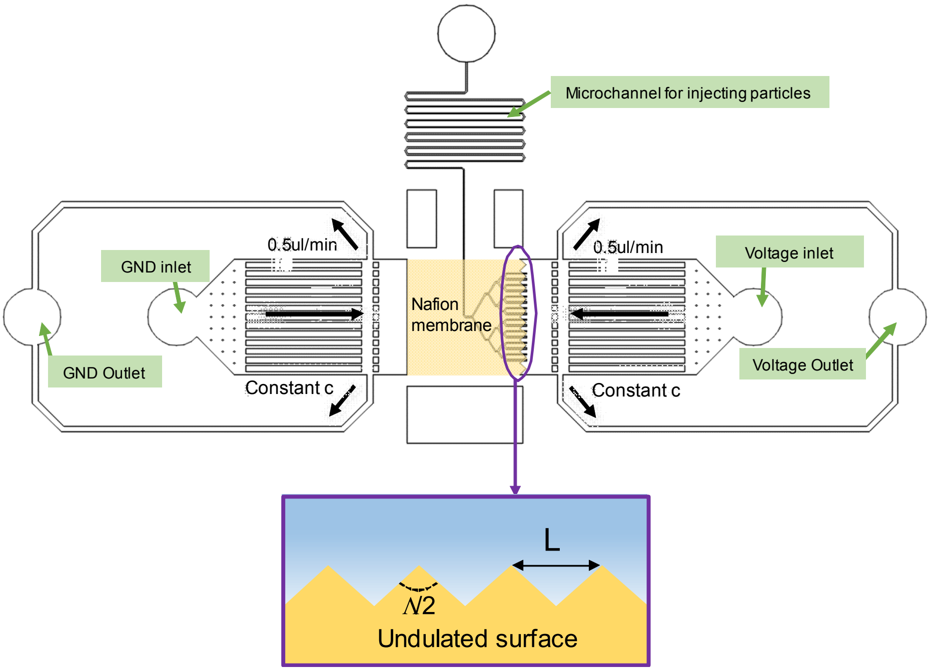

Figure 4.4 schematic image of the device and undulation surface configuration

4.3 Results and discussion

4.3.1 Visualization of the vortices of Dukhin's mode.

As shown in Figure 4.5, vortices of Dukhin's mode were observed when the 1V voltage was applied in 150 μm depth device. Since the electric field of the parallel to the inclined plane generates 1'st kind EOF, one vortex is formed for each inclined plane. These vortices enhance ion transportation. So that the overlimiting conductance of the device increased.

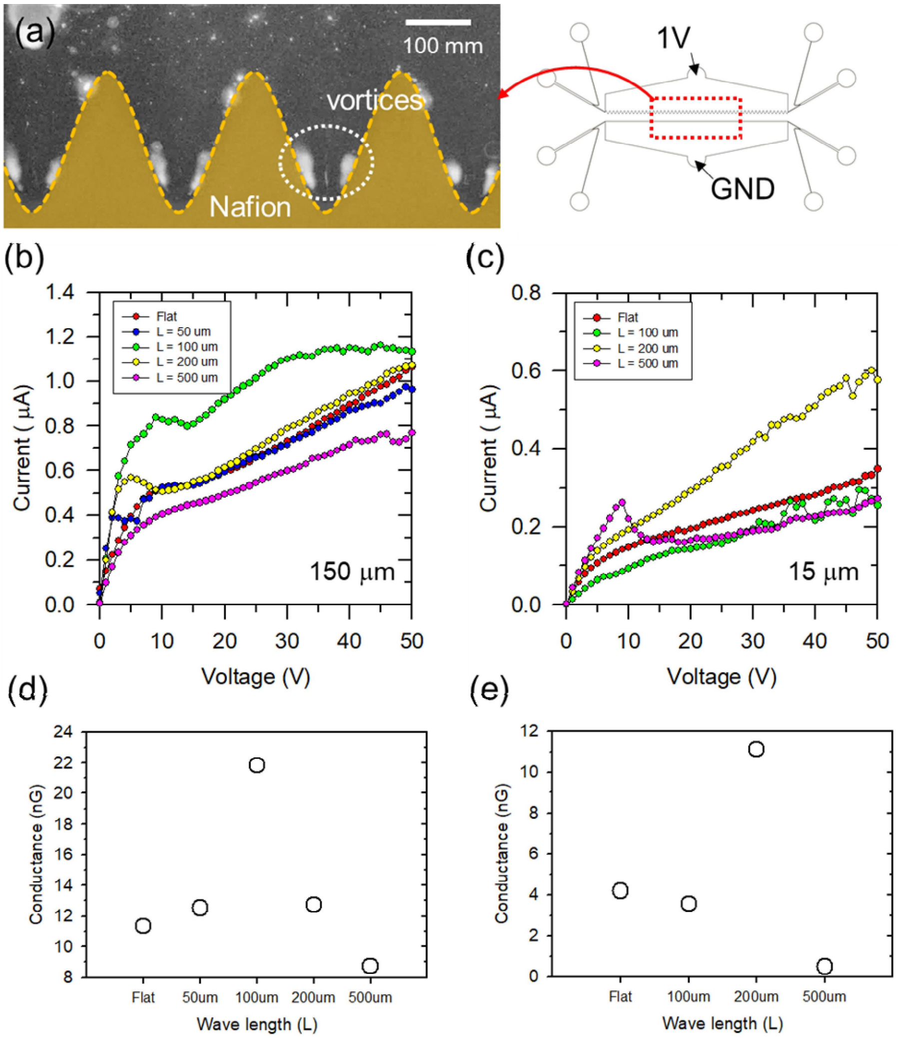

Figure 4.5 (a) electroconvective vortices near the undulation surface. I-V characteristics which had a characteristic length (b) 150 mm and (c) 15 mm. overlimting conductance depending on the wave length L at (d) 150 mm and (e) 15 mm

4.3.2 I-V characteristics of the undulation device

I-V characteristics at 15 μm and 150 μm depths of the undulation device were plotted as shown in Figure 4.5 (b) and (c). we analyzed slope of the overlimiting current between 15V and 20V. The voltage values were selected as the point at which stable electroconvection was occurring. As shown in Figure 4.5 (d) it was confirmed that the conductance value at 100 μm was peaked, similar to the theoretical expectation[34, 96]. If the wavelength is extremely large, Rubinstein's mode become more dominant than Dukhin's mode, and even if the wavelength is extremely small, it will be close to flat, and the Rubinstein's mode become more dominant. Therefore, the undulation effect may peak at the midpoint. In the case of device with a depth of 15 μm, Electro osmotic instability effect was reduced and convection was suppressed by depth, so we expect that the undulation effect (which is enhance the overlimiting conductance) was reduced. In the experiment, slightly different graph was appeared as shown in Figure 4.5 (e). First, the conductance of device with wavelength 100 μm was smaller than that of device with flat. The peak value was observed at the wavelength of 200 μm and the extremely small value was appeared at device with 500 μm. we thought that the 15 μm depth allowed 1st kind EOF such as Dukhin's mode vortices. Therefore, undulation effect which enhance the overlimiting current was also observed in 15 μm depth. To reduce the undulation effect, characteristic length of the device must be reduced under the 15 μm

4.4 Conclusions

The overlimting current is important factor of the fluidic platform imvolving permselective membrane. In particular, overlimting current could enhance the electrical power efficiency of the system such as fuel cell, electrodialysis, capacitive deionization, *etc* so that many researchers studied about the reason of overlimiting current. The electroconvection is the one of the cause of overlimiting current and Rubinstein mode and Duckhin's mode are two reasons of the electroconvection. In this work, Duckhin's mode electroconvection was investigated with the characteristic length 150 μm and 15 μm. Although several studies have been showed that overlimitig current was enhanced by using undulated surfaced platforms, these studies had a limitation that it has been studied only in the EOI regime with the characteristic length of 150 μm or more. At 150 μm depth, overlimiting conductance increased in the platforms with an undulation surface compared to flat ones. At 15 μm depths, overlimiting conductance was not changed much compared to when it was flat, except when the undulation wave length was 200 μm. In the case of wavelength 200 μm, I-V chracteristics must be retested because of experimental error. Except for the 200 μm case, overlimting conductance exhibits similar values. It means that the electroconvection by Duckhin's mode was suppressed by low characteristic length scale. Further theoretical investigation is necessary to reveal exact mechanism of suppress of electroconvection.

.

Appendix

Appendix A as courtesy of Dr. Yeonsu Jeong and Dr. Hyomin Lee

Appendix A. Analytical and numerical solution of the CICP

A.1 Domain descriptions with governing equation

The numerical and analytical analyses were conducted for the following domain where CICP occurred. A microchannel with length L was filled with 1:1 electrolyte solution. One side of the microchannel was opened to a well-mixed reservoir with bulk concentration, c_0 (at $x = 0$), while the other side contacted ideal cation-selective surface (at $x = L$). Assuming ideal perm-selectivity allowed us to avoid complexity in describing the transport phenomena inside the membrane, [30, 35, 36, 95, 97] so that the domain from reservoir to the membrane surface became the region of interest to be theoretically investigated. Since the streaming potential generated by the imbibition through the membrane was negligible, the effects of surface conduction and electroosmotic flow on the CICP were not considered. Therefore, the domain was simplified as 1-dimensional configuration.

In general, the transport of ionic species along the x-axis is governed by the Nernst-Planck equation,

$$\frac{\partial c_i}{\partial t} = -\frac{\partial J_i}{\partial x} \tag{A.1}$$

where t is the time, ci is the concentration of *i*-th species, and J_i is the ionic molar flux of *i*-th species along the x-axis. In accordance with transport mechanisms6, the ionic flux, J_i was given by

$$J_i = -D_i \frac{\partial c_i}{\partial x} - \frac{z_i F D_i}{RT} c_i \frac{\partial \psi}{\partial x} + c_i u \tag{A.2}$$

where D_i is the diffusivity of *i*-th species, F is the Faraday constant, R is the gas constant, and T is the absolute temperature, ψ is the electric potential, and u is the flow velocity of x-direction. In equation (A.2), each term on the right-hand side corresponds to transport mechanism due to diffusion, electro-migration, and convection, respectively. Although CICP experiments were conducted without any electric power source, the term of electro-migration should be considered to describe the electric interactions between ionic species. Thus, the interactions were explained by the Poisson equation,

$$-\varepsilon_f \frac{\partial^2 \psi}{\partial x^2} = F\left(c_+ - c_-\right) \tag{A.3}$$

where ε_f is the electrical permittivity of the electrolyte solution, and c_+ and c_- are the concentration of cation and anion, respectively. The Convective component of the ionic flux was usually obtained by solving the Stokes equations and the continuity equation with coupled partial differential equations (A.1) ~ (A.3). However, in this work, we adopted the simplified approach suggested by Dhopeshwarkar et al[98] to avoid mathematical complication. Since the effective convective transport was induced by the imbibition into the membrane, the flow velocity in microchannel (u) was related to the imbibition rate (u_{imb}) as

$$u = \phi_p u_{imb} \tag{A.4}$$

where ϕ_p is the porosity of the membrane which was assumed to consist of a bundle of cylindrical capillaries. Equation (A.4) was derived from the fact that the flow rate in the whole system should be uniform. This imbibition rate was the driving force for CICP, while the driving force of conventional ICP platforms was usually the difference of applied electric potentials.

Detailed boundary conditions at the reservoir bulk ($x = 0$) and the cation-selective surface ($x = L$) to describe the CICP would be discussed in the following sections.

A.2 Derivation of analytical solutions for steady state CICP

Since each ionic flux of *i*-th species was constant over the domain in the steady state, the Nernst-Planck equation is reduced to simplified balance equations as

$$J_+ = -D_+ \frac{\mathrm{d}c_+}{\mathrm{d}x} - \frac{FD_+}{RT} c_+ \frac{\mathrm{d}\psi}{\mathrm{d}x} + c_+ u \tag{A.5}$$

and

$$J_- = -D_- \frac{\mathrm{d}c_-}{\mathrm{d}x} + \frac{FD_-}{RT} c_- \frac{\mathrm{d}\psi}{\mathrm{d}x} + c_- u \tag{A.6}$$

for 1:1 electrolyte solution. For simplicity, thin double layers and electroneutrality ($c_+ = c_- = c$) were assumed in the microchannel as the domain. In addition, the diffusivity of each ionic species was fixed to the same value, ($D_+ = D_- = D$). For the ideal cation-selective surface, no anion flux existed over the microchannel. As a result, the above equations were rewritten as

$$J_+ = -D \frac{\mathrm{d}c}{\mathrm{d}x} - \frac{FD}{RT} c \frac{\mathrm{d}\psi}{\mathrm{d}x} + cu \tag{A.7}$$

and

$$0 = -D \frac{\mathrm{d}c}{\mathrm{d}x} + \frac{FD}{RT} c \frac{\mathrm{d}\psi}{\mathrm{d}x} + cu \tag{A.8}$$

Combining equations (A.7) and (A.8) yielded

$$J_{+} = -2D\frac{\mathrm{d}c}{\mathrm{d}x} + 2cu \tag{A.9}$$

while subtracting equation (A.8) from equation (A.7) yielded

$$J_{+} = -2\frac{DFc}{RT}\frac{\mathrm{d}\psi}{\mathrm{d}x} \tag{A.10}$$

The equations (A.9) and (A.10) were further simplified by non-dimensionalization with

$$\widetilde{x} \equiv \frac{x}{L},\ \widetilde{c} \equiv \frac{c}{c_0},\ \widetilde{\psi} \equiv \frac{F\psi}{RT},\ \widetilde{J} \equiv \frac{LJ_{+}}{2Dc_0},\ \text{and } \mathrm{Pe} \equiv \frac{uL}{D} \tag{A.11}$$

where Pe is known as the Péclet number, the ratio of a convective transport rate and a diffusive transport rate. Consequently, non-dimensional forms of equation (A.9) and (A.10) were, respectively,

$$\widetilde{J} = -\frac{\mathrm{d}\widetilde{c}}{\mathrm{d}\widetilde{x}} + \mathrm{Pe}\ \widetilde{c} \tag{A.12}$$

and

$$\widetilde{J} = -\widetilde{c}\,\frac{d\widetilde{\psi}}{d\widetilde{x}}. \tag{A.13}$$

Because $\widetilde{c}$ = 1 and $\widetilde{\psi}$ = 0 at $\widetilde{x}$ = 0 equations, (A.12) and (A.13) could be integrated under constant $\widetilde{J}$ which was induced by imbibition through the membrane. Therefore, the following analytical solutions could be obtained with respect to the concentration and the electric potential inside CICP layer as

$$\tilde{c} = \frac{\left(\mathrm{Pe} - \tilde{J}\right)\exp\left(\mathrm{Pe}\ \tilde{x}\right) + \tilde{J}}{\mathrm{Pe}} \tag{A.14}$$

and

$$\tilde{\psi} = -\mathrm{Pe}\ \tilde{x} + \ln\left[\frac{\left(\mathrm{Pe} - \tilde{J}\right)\exp\left(\mathrm{Pe}\ \tilde{x}\right) + \tilde{J}}{\mathrm{Pe}}\right]. \tag{A.15}$$

A.3 Analytical analysis for the formation of CICP

Although CICP experiments were conducted without any electric power source, the electric interactions between ionic species should appear in terms of electro-migration. Pe is the Péclet number which is the ratio of a convective transportation to a diffusive transportation (*uL/D* in this system). Simple analytical solutions implied the most important parameters for enhancing the desalination efficiency near the membrane.

The experimental results showed that the electrolyte concentration was depleted near the membrane (i.e. the concentration gradient was negative, $\mathrm{d}c/\mathrm{d}x < 0$) so that $\widetilde{J}$ was greater than Pe, since $\mathrm{d}\widetilde{c}/\mathrm{d}\widetilde{x}$ was equal to (Pe - $\widetilde{J}$) exp[Pe $\widetilde{x}$]. Appendix Figure A.1 (a) and A.1 (b) showed the concentration profile plots at the different physicochemical parameters, while Pe and $\widetilde{J}$ were fixed at 0.1 for each plot because the microfluidic device had Pe of ~0.1 with $D \sim O(10^{-9})$ m^2/sec, L (the length of the microchannel) ~ O(1) mm and u (a flow velocity due to an imbibition) ~ O(10) μm/min. The physical intuitions from the plots were such that (1) higher $\widetilde{J}$ and (2) lower Pe give a severer depletion. Since $\widetilde{J}$ was proportional to the charge imbalance ($\widetilde{J} = -\widetilde{c}\dfrac{d\widetilde{\psi}}{d\widetilde{x}}$, See equation (A.10) and (A.13) in Supporting information), the higher perm-selectivity would enhance the formation of the ion depletion zone. This was also confirmed in Figure 10 (b) and 10 (c). By comparing the plots, the higher composition of the charged group (AA) led to a stronger depletion behavior which implied a longer duration. However, an excess amount of the charged group in the hydrogel resulted in a brittle structure so that one should tweak the composition as one's discretion. For latter case, a diffusion limited system (*i.e.* lower Pe) drove the depletion phenomenon more efficiently.

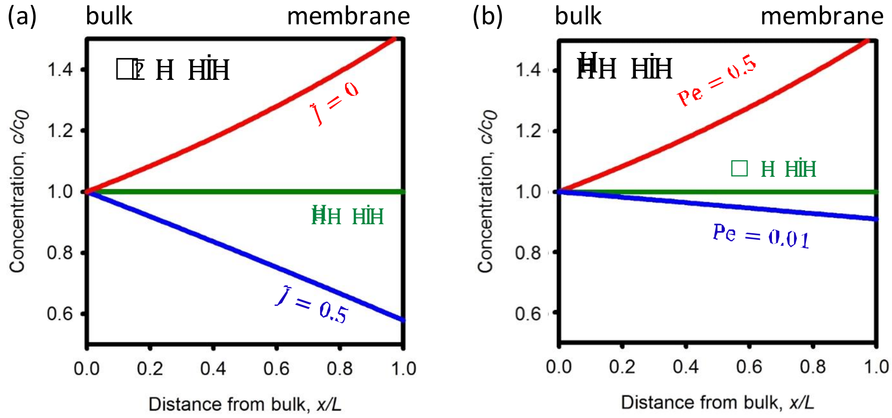

Appendix Figure A.1. The plots of normalized concentration inside the ion-depletion zone with fixed (a) Pe at 0.1 and (b) ionic flux at 0.1.

A.4 Numerical method for CICP analysis

Numerical simulations were conducted by COMSOL Mutiphysics 4.4, a commercial finite element method tool, under 1-dimensional domain and transient analysis mode. The domain was discretized into 1,000 elements, with finer meshes in proximity to a membrane surface. In order to carry out a qualitative analysis for CICP system, we assumed that the diffusion time scale (τ_D) and the porosity (ϕ_p) were 500 seconds and 0.1, respectively. In addition, the non-dimensional Debye length and Donnan equilibrium concentration were set to be 0.01 and 5. From Washburn's equation[45], the imbibition rate is infinite at t = 0 sec so that the initial conditions cannot be defined. To avoid this problem, a transient analysis was conducted from t = 1 sec rather than from t = 0 sec. The time step and the termination time were set to be 1 sec and 3,600 sec, respectively.

A.5 The formulation of transient model for CICP

The imbibition into a capillary tube is described by Washburn's equation[45] which was

$$L_{imb}{}^{2} = \frac{\gamma\, d_{cap}}{4\eta} t \tag{A.16}$$

where L_{imb} is imbibition length, γ is the surface tension of water/capillary wall/air interface, and d_{cap} is the diameter of capillary. By differentiating equation (A.16), the imbibition rate was obtained as following

$$u_{imb} = \sqrt{\frac{S}{4t}} \tag{A.17}$$

where S is defined by $\gamma\, d_{cap} \,/\, 4\eta$. Because u_{imb} as the source of CICP was proportional to $t^{-0.5}$, the thickness of CICP layer induced by imbibition into the membrane would be decreased as time passed.

The spatiotemporal concentration profile inside the CICP layer was obtained by the following non-dimensional forms of equation (A.2) ~ (A.3) with appropriate boundary conditions.

$$\frac{\partial}{\partial \tilde{x}}\left(-\frac{\partial \tilde{\psi}}{\partial \tilde{x}}\right) = \frac{\tilde{c}_{+} - \tilde{c}_{-}}{2\tilde{\lambda}_{D}} \tag{A.18}$$

and

$$\frac{\partial \tilde{c}_i}{\partial \tilde{t}} = -\frac{\partial}{\partial \tilde{x}}\left(-\frac{\partial \tilde{c}_i}{\partial \tilde{x}} - z_i \tilde{c}_i \frac{\partial \tilde{\psi}}{\partial \tilde{x}} + \phi_p \tilde{c}_i \tilde{u}_{imb}\right) \tag{A.19}$$

where the characteristic scales of c_i, ψ, and x were denoted in equation (A.11), the characteristic time was chosen as the diffusion time scale, τ_D defined as L^2 / D, and the characteristic velocity was set to be D / L. In equation (A.18), $\tilde{\lambda}_D$ is the non-dimensional Debye length defined as

$$\tilde{\lambda}_D = \frac{1}{L}\sqrt{\frac{\varepsilon_f RT}{2z^2F^2c_0}} \tag{A.20}$$

for z:z electrolyte solution. At the reservoir bulk ($\tilde{x} = 0$), the following boundary conditions should be satisfied.

$$\tilde{\psi} = 0 \text{ and } \tilde{c}_i = 1. \tag{A.21}$$

At the ideally cation-selective surface ($\tilde{x} = 1$), the cation flux through the ionic hydrogel pad was generated only by the imbibition,

$$-\frac{\partial \tilde{\psi}}{\partial \tilde{x}} = \frac{\partial \ln \tilde{c}_+}{\partial \tilde{x}}, \tag{A.22}$$

and the perm-selectivity was described by

$$\tilde{c}_+ = \tilde{N} \tag{A.23}$$

and

$$-\frac{\partial \tilde{c}_-}{\partial \tilde{x}} + c_- \frac{\partial \tilde{\psi}}{\partial \tilde{x}} + \phi_p \tilde{c}_i \tilde{u}_{imb} = 0. \tag{A.24}$$

Equation (A.22) implied that a gradient of electrochemical potential ($\nabla(\tilde{\psi} + \ln \tilde{c}_+) = 0$) would be zero, so that only a convective transportation into the membrane contributed to form the CICP layer. The Donnan equilibrium concentration[30, 35] inside the nanoporous membrane was described by equation (A.23) and equation (A.24), which impeded that anion flux into the membrane should be zero due to ideal cation-selectivity. Equations (A.18) ~ (A.19) with boundary conditions (A.21) ~ (A.24) were solved numerically.

A.6 Numerical analysis for restoration phase

Through the transient model, the dynamic changes of CICP layer were investigated. With chosen parameters in Numerical method section, the depletion phase as depicted in Appendix Figure A.2 (a) lasted for $\tilde{t} \sim 0.4$ when the non-dimensional imbibition parameter $\tilde{S}$ was 100 (normalized by L^2 / $D^2\tau_D$). However, beyond this point, the phase transited to the restoration phase as shown in Appendix Figure A.2 (b) because of the decreased imbibition rate. These simulation results largely corresponded to the experimental results in Figure 11 (a)~ 11 (c). Although the imbibition rate decreased gradually in both the depletion and the restoration phase, the contribution of the imbibition in the depletion phase was still larger than the dissipation of ionic species induced by a diffusion. Briefly, the depletion phase initially appeared (*i.e.* the imbibition rate > the dissipation) and changed into the restoration phase (*i.e.* the imbibition rate < the dissipation).

In Appendix Figure 4 (c), the minimum cation concentrations inside the depletion zone were plotted with varying imbibition parameters, $\tilde{S}$, as a function of time. The parameter could be tuned by the absorbing capability of the ionic hydrogel. The imbibition parameter was defined by $(\gamma\, d_{cap})$ / $(4D\eta)$ where γ is the surface tension, d_{cap} is the diameter of a capillary, and η is the dynamic viscosity of the fluid. The increase of γ and d_{cap} or the decrease of η was one of the solutions to enhancing the imbibition rate. While the Washburn's equation has been known to describe the imbibition through a single capillary tube, recent reports [99-101] suggested that the functional form of the imbibition in the case of a capillary network also followed the Washburn's equation. Nevertheless, the transient analysis with arbitrary $\tilde{S}$ provided the insight for understanding the transition from the depletion phase to the restoration phase. Larger $\tilde{S}$ generated a higher imbibition rate which was enough to overcome the dissipation so that the depletion

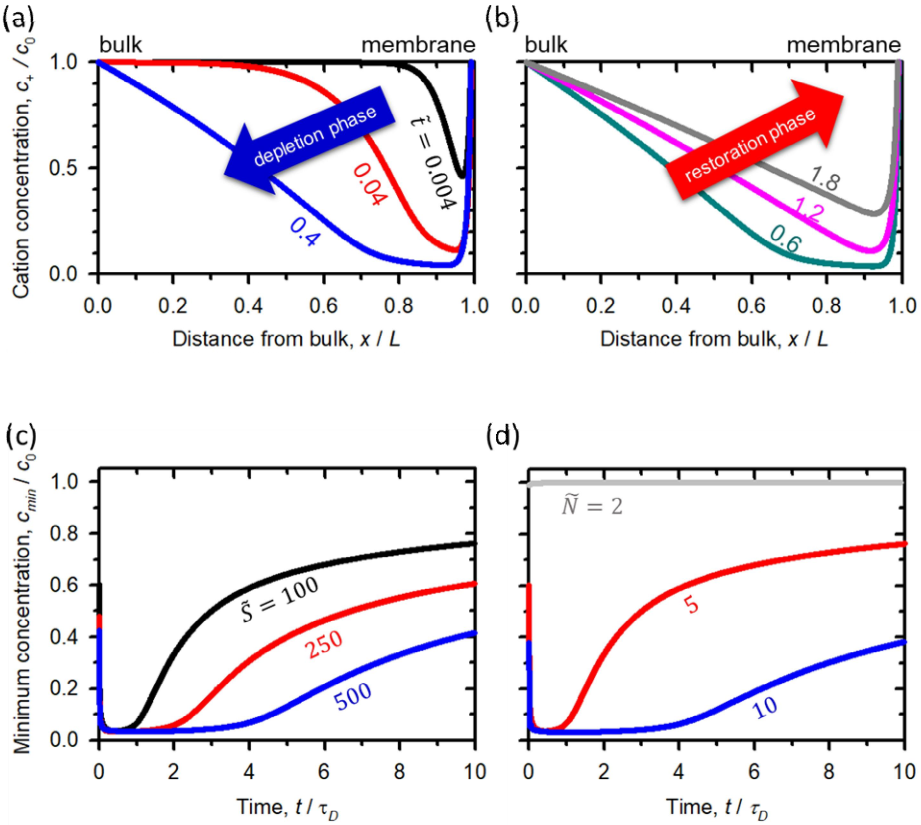

Appendix Figure A.2 The depletion and the restoration phase of CICP. Cation concentration profiles inside the CICP zone at (a) the depletion phase and (b) the restoration phase. The minimum cation concentrations inside the ion-depletion zone with varying (c) imbibition parameters and (d) Donnan equilibrium concentrations.

phase sustained longer. Moreover, the ionic hydrogel of a higher charges had more sustainable depletion phase by comparing Figure 11 (b) and 11 (c). The hydrogel used in Figure 11 (c) had the higher composition of a charged group, AA. In this theoretical model, the non-dimensional Donnan equilibrium concentration ($\widetilde{N}$) was related to the intrinsic charge of membrane. The membrane possessing a higher charge generated a higher ionic flux through the membrane, so that the depletion phase could last longer as shown in Appendix Figure A.2 (d) with fixed $\widetilde{S}$ at 100.

Appendix B as courtesy of Mr. Sungjun Hong and Dr. Seok Young Son.

Appendix B. Hen egg yolk and albumen as a bio-based perm-selective membrane

B.1 Hen egg yolk and albumen as a perm-selective membrane

The second material is a hen egg. An albumen which is white part of an egg is similar to the physical morphology of a jelly like hydrogel. In addition, albumen has been used as a support medium in the electrophoresis of protein detection [102] and as nanoporous mats because of its nanopores which can confirm by SEM image[103]. A yolk which is yellow part of an egg forms a microparticle-like powder when it was heated [104]. When the microparticles are self-assembled, the holes between the closed packed particles form nanopores. Thus, these nanopores of albumen and yolk would be expected as nanoporous material in this work.

B.2 Egg device fabrication

Fabrication of the device using hen egg (named as “egg device”) as a nanoporous membrane for visualization and I-V curve was as follows. Each albumen and yolk are used as a nanoporous membrane. A T-shaped microchannel (100 μm (width) × 15 μm (depth)) together with air-valve microchannels for experimental easiness[105] was fabricated by a general PDMS fabrication method as shown in Appendix Figure B.1. (a). The T-shaped microchannel PDMS block which was punched by biopsy punch to create the hole (diameter: 1.5 mm) and glass slide were irreversibly bonded with oxygen plasma treatment. After bonding, albumen or yolk was injected into the microchannel up to the predetermined boundary. Then, the device was heated at 120 °C for complete denaturation. After heating, pipette tips served as reservoirs were inserted into the hole of the PDMS block. KCl solution (1 mM) was filled in the reservoirs. Two Ag electrodes were set to apply an external voltage to the reservoir.

Fabrication of the device using egg for conductance profile was as follows. PDMS block which has rectangular hole (15 mm × 10 mm) and thickness of 1.5 mm was irreversibly bonded with glass slide using O_2 plasma to fabricate container as shown in Appendix Figure B.2. Aluminum foil was bonded at the edge (10 mm side) of the container to apply electric field uniformly. Egg yolk or albumen was poured in the container and heated at 120 °C for complete denaturation. For the conductance measurement of albumen and yolk, the device was immersed in the KCl solution at a concentration ranging from 0.1 mM to 1 M for more than 24 hours. At each concentration, the voltage was increased from -0.2 V to -0.2 V in 0.04 V increments, and the interval between each voltage was 1 sec. The current values at each step were recorded by customized Labview program. The conductance values were then calculated from the slope of the I-V curve.

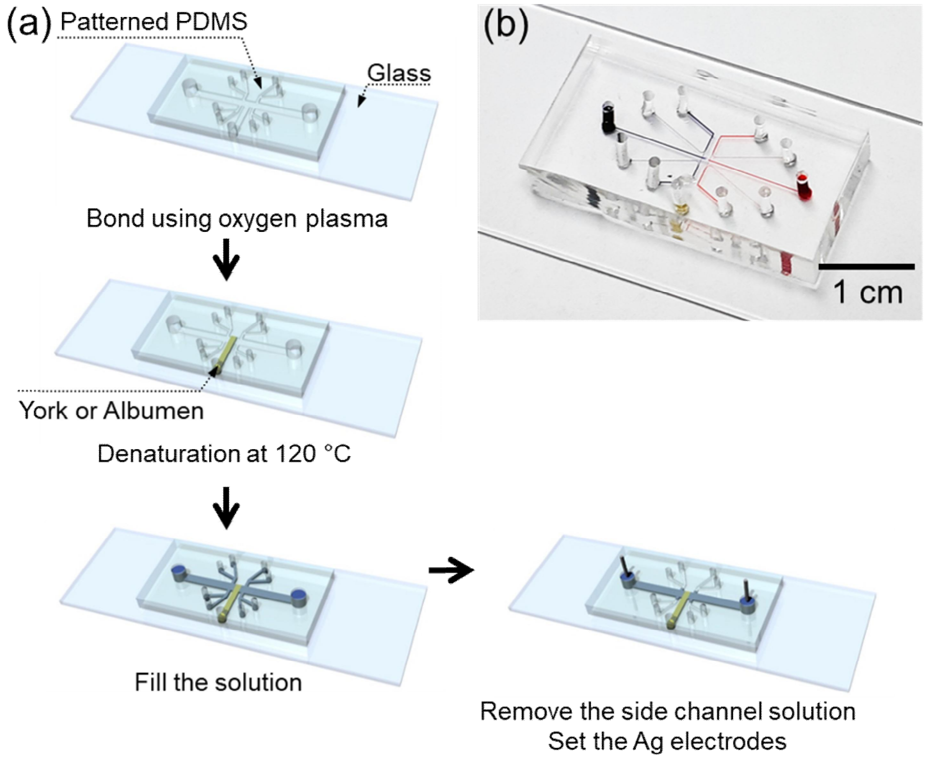

Appendix Figure B.1. (a) The fabrication process of the egg device. (b) The photo of assembled egg device

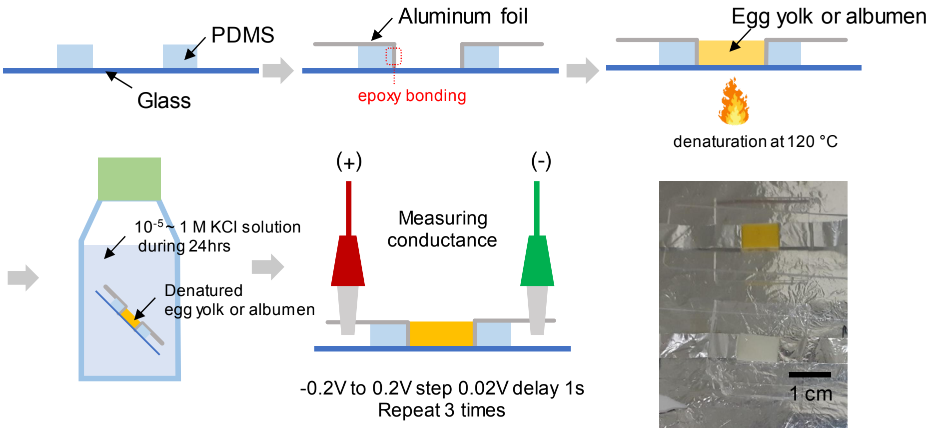

Appendix Figure B.2. schematic diagram of the conductance measurement experimental process of the egg devices and photo of assembled egg conductance devices

B.3 Materials and experimental setups of egg deivce

For visualization experiments for the egg device, KCl solution (1 mM) with Alexa 488 fluorescent dye (1 μM) was used for electrolyte. 30 V of DC bias was applied to the device. The propagation of ICP layer were captured by an inverted fluorescent microscope and CellSens program.

For the I-V characteristic measurement of the egg device, KCl solution (1 mM) was used for electrolyte. The voltage was applied stepwise from 0 V to 20 V at 0.1 V/sec. The current values at each step were recorded by customized Labview program.

B.4 The characteristics of egg deivce

The same procedure was conducted in the egg device in this section. External voltage of 30 V DC bias was applied to the device. As shown in Appendix Figure B.3. (a), the ion depletion zone and the ion enrichment zone were formed at the anodic and cathodic side of egg membrane, respectively, which means that the albumen and the yolk are not only a medium of mass transfer but also permselective nanoporous membrane.

Also, the devices had the unique I-V responses as similar as the nail device as shown in Appendix Figure B.3 (b). In this device, external voltage was swept from 0 V to 20 V at 0.1 V/sec. Interestingly, similar I-V characteristics were observed in both cases of the yolk and albumen since egg device had long microchannel and short membrane, meaning that the ohmic loss inside the microchannel was dominant in such low concentration of 1 mM[106] . Thus, the similar ohmic region of both albumen and yolk was observed in Appendix Figure B.3 (b). The egg yolk and albumen membrane caused a limiting current and overlimiting current as well.

The quantitative properties of the yolk and albumen membrane could be analyzed by similar manner in previous section. As shown in Figure B.3 (c), the conductance-concentration plots of albumen or yolk membrane also showed two different regimes. See supporting information for the fabrication and measurement method of egg device. The converged value of the conductance of albumen at low concentration was higher than that of yolk as shown. This means that the N_w of the albumen was higher than that of yolk. α was estimated by 0.2 C·m/mol in both egg albumen and yolk. N_w of the albumen was estimated by 33 mM and that of the yolk was estimated by 15 mM. (Equivalent hydrodynamic radius a of the albumen and yolk was assumed as 20 nm and 120 nm, respectively.) [103, 107, 108] Using the value of the N_w, the surface charge of the albumen and yolk was estimated by - 16 mC/m^2 and - 43 mC/m^2, respectively. These values were higher than the surface

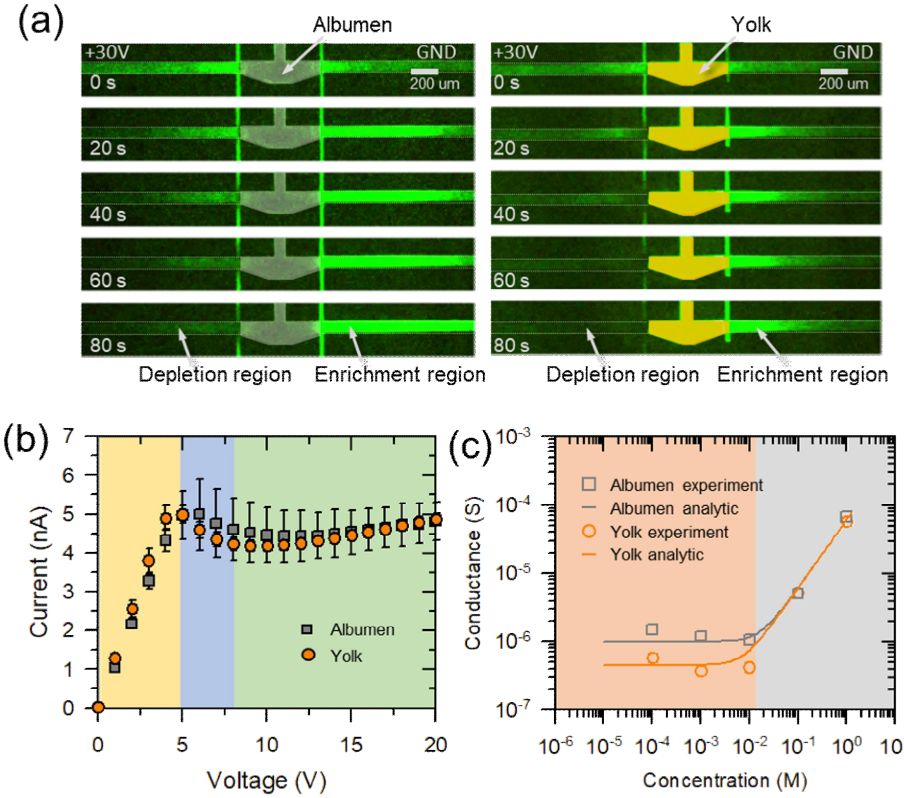

Appendix Figure B.3. (a) The visualization of an ion depletion zone and an ion enrichment zone resulted from ICP phenomenon using egg devices. (b) I-V characteristics of egg devices. (c) Conductance profile of the egg devices.

charge of silicon (-15 mC/m^2) so that the permselectivity of albumen and yolk is comparable with silicon nanochannel. These conductance values and Donnan concentrations were organized in Table 3.1.

B.5 ICP demonstration using egg nanojunction in paper device

ICP phenomenon in a paper-based micro/nanofluidic device using hen egg yolk and albumen was demonstrated in this section for biodegradable and eco-friendly applications. Paper consisted of micron-size cellulose usually used as a microchannel because it has not only micro-sized holes, but it also has a capillary force to spontaneously pump a sample fluid[69, 72]. Since denatured hen egg yolk and albumen has nanopores, micro/nano-fluid dynamics occurs in this paper-based device as similar as micro/nano-channel-based devices.

The paper-based ICP device was fabricated by cellulose paper (180 μm of thickness and a mean pore diameter of 3 μm, Whatman grade 1, Sigma-Aldrich, USA) and 10 mL-tube caps which are used as reservoir in the Appendix Figure B.4 (a)-(i). The tube caps were glued on a slide glass as a supporter. A commercial wax printer (ColorQube 8570, FUJI Xerox) was utilized for printing hydrophobic guide of microchannel (black part of paper in Appendix Figure B.4 (a)-(ii)). Albumen or yolk was dropped at the center of paper for forming a cation-selective membrane (Appendix Figure B.4 (a)-(ii)). After resting 5 minutes for complete absorption into the paper, the patterned paper was heated at 120 ºC for 1 min. The fabricated devices were dried in petri dishes with cover at room temperature. Ag electrodes were inserted into cathode and anode (Appendix Figure B.4 (a)-(iii)) and connected to a power supply (Keithley 236, Keithley Instruments, USA). Fabricated device is shown in Appendix Figure B.4 (b). For the visualization experiments for the paper device, KCl (1 mM) with Alexa 488 fluorescent dye (1 μM) were used as electrolyte and tracer, respectively. After dropping the electrolyte solution on the paper, one need to wait until the paper is completely wetted by capillarity. 100 V of

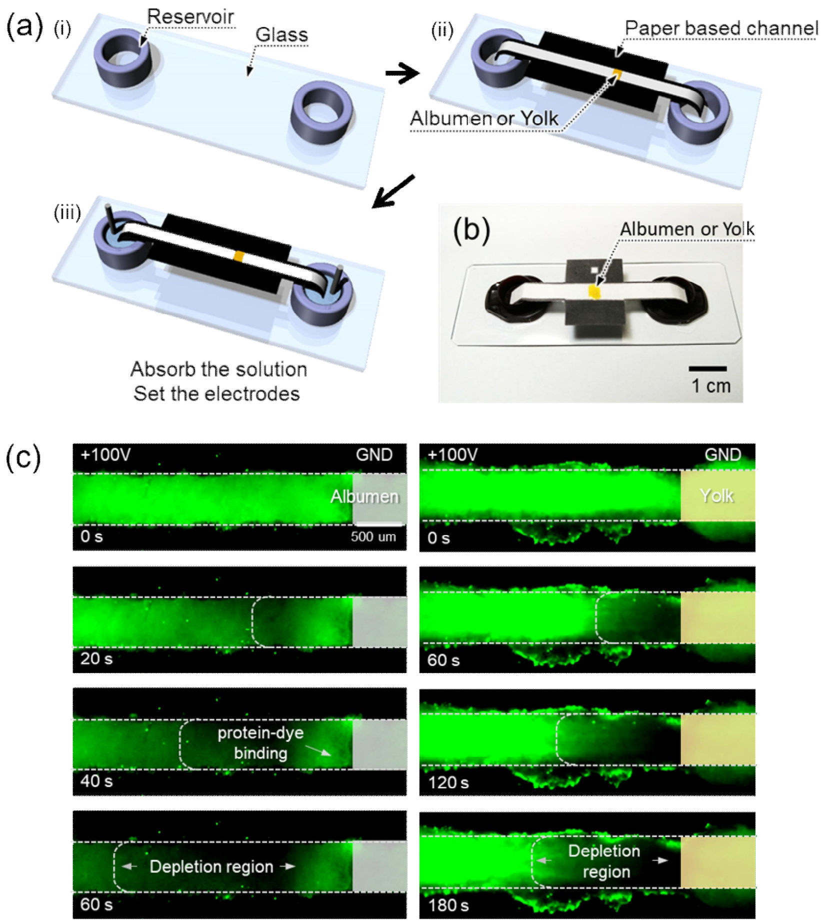

Appendix Figure B.4 (a) The fabrication process of the paper based ICP device using egg membrane. (b) The photo of assembled paper based ICP device. (c) The visualization of ICP phenomenon using paper based ICP device..

DC bias was applied to the device. The propagation of ICP layer were captured by an inverted fluorescent microscope and CellSens program.

As shown in Appendix Figure B.4 (c), fluorescent dye molecules which represent movement of ions depleted near the yolk membrane. We confirmed that ICP phenomenon occurred in paper-based devices with both albumen and yolk membrane. However, in the case of the albumen membrane, fluorescent dye molecules in the immediate vicinity of the membrane were not depleted as shown. This unexpected fluorescent signal could be explained by protein-dye binding. Anionic florescent dyes (Alexa 488) which is used in this work, strongly bind to heat-denatured ovalbumin which is the main protein found in egg albumen, making up approximately 55% of the total protein[109]. Since the cross-sectional area of the membrane boundary of paper device was much larger than that of PDMS device, binding effect only occurs in paper device and was negligible in PDMS device. Nevertheless, the depletion region was observed near both yolk and albumen membrane, so that the yolk and albumen nano membrane imbedded paper-based media could be utilized for the element of the micro/nanofluidic biodegradable and eco-friendly applications.

Bibliography

1. Kirby, B.J., *Micro-and nanoscale fluid mechanics: transport in microfluidic devices*. 2010: Cambridge university press.
2. Tanaka, Y., *Ion Exchange Membranes: Fundamentals and Applications, Series 12.* Membrane Science and Technology: Elsevier, Netherlands, 2007.
3. Mauritz, K.A. and R.B. Moore, *State of understanding of Nafion.* Chemical reviews, 2004. **104**(10): p. 4535-4586.
4. Song, H., et al., *Nafion-film-based micro–nanofluidic device for concurrent DNA preconcentration and separation in free solution.* Microfluidics and nanofluidics, 2014. **17**(4): p. 693-699.
5. Huh, K., et al., *Surface Conduction and Electroosmotic Flow around Charged Dielectric Pillar Arrays in Microchannels.* Lab on a Chip, 2020.
6. Choi, J., et al., *Nanoelectrokinetic Selective Preconcentration Based on Ion Concentration Polarization.* BioChip Journal, 2020: p. 1-10.
7. Ko, S.H., et al., *Nanofluidic preconcentration device in a straight microchannel using ion concentration polarization.* Lab on a Chip, 2012. **12**(21): p. 4472-4482.
8. Dong, L., et al., *Adaptive liquid microlenses activated by stimuli-responsive hydrogels.* Nature, 2006. **442**(7102): p. 551-554.
9. Park, T.G. and A.S. Hoffman, *Synthesis and characterization of pH□and/or temperature□sensitive hydrogels.* Journal of Applied Polymer Science, 1992. **46**(4): p. 659-671.
10. Kim, P., et al., *Stabilization of ion concentration polarization using a heterogeneous nanoporous junction.* Nano letters, 2010. **10**(1): p. 16-23.
11. Kim, S.J., Y.-A. Song, and J. Han, *Nanofluidic concentration devices for biomolecules utilizing ion concentration polarization: theory, fabrication, and applications.* Chemical Society Reviews, 2010. **39**(3): p. 912-922.
12. Son, S.Y., et al., *Engineered nanofluidic preconcentration devices by ion concentration polarization.* BioChip Journal, 2016. **10**(4): p. 251-261.
13. Kim, B., et al., *Tunable ionic transport for a triangular nanochannel in a polymeric nanofluidic system.* Acs Nano, 2013. **7**(1): p. 740-747.
14. Heo, J., et al., *Ultra-high-aspect-orthogonal and tunable three dimensional polymeric nanochannel stack array for BioMEMS applications.* Nanoscale, 2014. **6**(16): p. 9681-9688.
15. Chen, G., et al., *A Highly Conductive Cationic Wood Membrane.* Advanced Functional Materials, 2019. **29**(44): p. 1902772.
16. Choi, E., et al., *An electrokinetic study on tunable 3D nanochannel networks constructed by spatially controlled nanoparticle assembly.* Lab on a Chip, 2015. **15**(2): p. 512-523.
17. Kim, S.J., et al., *Direct seawater desalination by ion concentration polarization.* Nature nanotechnology, 2010. **5**(4): p. 297-301.
18. Kwak, R., et al., *Microscale electrodialysis: Concentration profiling and vortex visualization.* Desalination, 2013. **308**: p. 138-146.
19. Nikonenko, V.V., et al., *Desalination at overlimiting currents: State-of-the-art and perspectives.* Desalination, 2014. **342**: p. 85-106.
20. Shannon, M.A., et al., *Science and technology for water purification in the coming decades*, in *Nanoscience and technology: a collection of reviews from nature Journals*. 2010, World Scientific. p. 337-346.
21. Kwak, R., K.M. Lim, and J. Han, *Shear flow of an electrically charged fluid by ion concentration polarization: Scaling laws for electroconvective vortices.* Physical review letters, 2013. **110**(11): p. 114501.

22. Deng, D., et al., *Overlimiting current and shock electrodialysis in porous media.* Langmuir, 2013. **29**(52): p. 16167-16177.
23. Deng, D., et al., *Water purification by shock electrodialysis: Deionization, filtration, separation, and disinfection.* Desalination, 2015. **357**: p. 77-83.
24. Pu, Q., et al., *Ion-enrichment and ion-depletion effect of nanochannel structures.* Nano letters, 2004. **4**(6): p. 1099-1103.
25. Kim, S.J. and J. Han, *Self-sealed vertical polymeric nanoporous-junctions for high-throughput nanofluidic applications.* Analytical chemistry, 2008. **80**(9): p. 3507-3511.
26. Fosdick, S.E., et al., *Bipolar electrochemistry.* Angewandte Chemie International Edition, 2013. **52**(40): p. 10438-10456.
27. Knust, K.N., et al., *Electrochemically mediated seawater desalination.* Angewandte Chemie International Edition, 2013. **52**(31): p. 8107-8110.
28. Leinweber, F.C. and U. Tallarek, *Nonequilibrium electrokinetic effects in beds of ion-permselective particles.* Langmuir, 2004. **20**(26): p. 11637-11648.
29. Höltzel, A. and U. Tallarek, *Ionic conductance of nanopores in microscale analysis systems: Where microfluidics meets nanofluidics.* Journal of separation science, 2007. **30**(10): p. 1398-1419.
30. Dydek, E.V., et al., *Overlimiting current in a microchannel.* Physical review letters, 2011. **107**(11): p. 118301.
31. Nam, S., et al., *Experimental verification of overlimiting current by surface conduction and electro-osmotic flow in microchannels.* Physical review letters, 2015. **114**(11): p. 114501.
32. Kim, S.J., et al., *Concentration polarization and nonlinear electrokinetic flow near a nanofluidic channel.* Physical review letters, 2007. **99**(4): p. 044501.
33. Rubinstein, S.M., et al., *Direct observation of a nonequilibrium electro-osmotic instability.* Physical review letters, 2008. **101**(23): p. 236101.
34. Pundik, T., I. Rubinstein, and B. Zaltzman, *Bulk electroconvection in electrolyte.* Physical Review E, 2005. **72**(6): p. 061502.
35. Green, Y. and G. Yossifon, *Dynamical trapping of colloids at the stagnation points of electro-osmotic vortices of the second kind.* Physical Review E, 2013. **87**(3): p. 033005.
36. Rubinstein, I. and B. Zaltzman, *Electro-osmotically induced convection at a permselective membrane.* Physical Review E, 2000. **62**(2): p. 2238.
37. Ko, S.H., et al., *Massively parallel concentration device for multiplexed immunoassays.* Lab on a Chip, 2011. **11**(7): p. 1351-1358.
38. Cho, I., G.Y. Sung, and S.J. Kim, *Overlimiting current through ion concentration polarization layer: hydrodynamic convection effects.* Nanoscale, 2014. **6**(9): p. 4620-4626.
39. Parida, A.K. and B. Jha, *Salt tolerance mechanisms in mangroves: a review.* Trees, 2010. **24**(2): p. 199-217.
40. Beebe, D.J., et al., *Functional hydrogel structures for autonomous flow control inside microfluidic channels.* Nature, 2000. **404**(6778): p. 588-590.
41. Lee, K.Y. and D.J. Mooney, *Hydrogels for tissue engineering.* Chemical reviews, 2001. **101**(7): p. 1869-1880.
42. Cai, S. and Z. Suo, *Equations of state for ideal elastomeric gels.* EPL (Europhysics Letters), 2012. **97**(3): p. 34009.
43. Marcombe, R., et al., *A theory of constrained swelling of a pH-sensitive hydrogel.* Soft Matter, 2010. **6**(4): p. 784-793.
44. Suzuki, A. and T. Hara, *Kinetics of one-dimensional swelling and shrinking of polymer gels under mechanical constraint.* The Journal of Chemical Physics, 2001. **114**(11): p. 5012-5015.
45. Dullien, F.A., *Porous media: fluid transport and pore structure*. 2012: Academic press.

46. Kim, S.J., L.D. Li, and J. Han, *Amplified electrokinetic response by concentration polarization near nanofluidic channel.* Langmuir, 2009. **25**(13): p. 7759-7765.
47. Kim, S.J., et al., *Multi-vortical flow inducing electrokinetic instability in ion concentration polarization layer.* Nanoscale, 2012. **4**(23): p. 7406-7410.
48. Lee, S.-H., et al., *Sub-10 nm transparent all-around-gated ambipolar ionic field effect transistor.* Nanoscale, 2015. **7**(3): p. 936-946.
49. Kwak, R., S.J. Kim, and J. Han, *Continuous-flow biomolecule and cell concentrator by ion concentration polarization.* Analytical chemistry, 2011. **83**(19): p. 7348-7355.
50. Eijkel, J.C. and A. Van Den Berg, *Nanofluidics: what is it and what can we expect from it?* Microfluidics and Nanofluidics, 2005. **1**(3): p. 249-267.
51. Schoch, R.B., *Transport phenomena in nanofluidics: From ionic studies to proteomic applications*. 2006, PhD Thesis.
52. Stein, D., M. Kruithof, and C. Dekker, *Surface-charge-governed ion transport in nanofluidic channels.* Physical Review Letters, 2004. **93**(3): p. 035901.
53. Mani, A., T.A. Zangle, and J.G. Santiago, *On the propagation of concentration polarization from microchannel− nanochannel interfaces Part I: analytical model and characteristic analysis.* Langmuir, 2009. **25**(6): p. 3898-3908.
54. Chang, H.-C., G. Yossifon, and E.A. Demekhin, *Nanoscale electrokinetics and microvortices: How microhydrodynamics affects nanofluidic ion flux.* Annual review of fluid mechanics, 2012. **44**: p. 401-426.
55. Bocquet, L. and E. Charlaix, *Nanofluidics, from bulk to interfaces.* Chemical Society Reviews, 2010. **39**(3): p. 1073-1095.
56. Van Honschoten, J.W., N. Brunets, and N.R. Tas, *Capillarity at the nanoscale.* Chemical society reviews, 2010. **39**(3): p. 1096-1114.
57. Piruska, A., et al., *Nanofluidics in chemical analysis.* Chemical Society Reviews, 2010. **39**(3): p. 1060-1072.
58. Levy, S.L. and H.G. Craighead, *DNA manipulation, sorting, and mapping in nanofluidic systems.* Chemical Society Reviews, 2010. **39**(3): p. 1133-1152.
59. Mark, D., et al., *Microfluidic lab-on-a-chip platforms: requirements, characteristics and applications*, in *Microfluidics based microsystems*. 2010, Springer. p. 305-376.
60. Li, X., et al., *Effect of surface modification on the stability and thermal conductivity of water-based SiO2-coated graphene nanofluid.* Thermochimica acta, 2014. **595**: p. 6-10.
61. Xie, Q., et al., *Fast water transport in graphene nanofluidic channels.* Nature nanotechnology, 2018. **13**(3): p. 238-245.
62. Kim, C.-C., et al., *Highly stretchable, transparent ionic touch panel.* Science, 2016. **353**(6300): p. 682-687.
63. Chen, Y.-Y., et al., *Preconcentration of diluted mixed-species samples following separation and collection in a micro–nanofluidic device.* Biomicrofluidics, 2016. **10**(1): p. 014119.
64. Choi, E., et al., *High current ionic diode using homogeneously charged asymmetric nanochannel network membrane.* Nano letters, 2016. **16**(4): p. 2189-2197.
65. Song, Y.-A., et al., *Tunable membranes for free-flow zone electrophoresis in PDMS microchip using guided self-assembly of silica microbeads.* Analytical chemistry, 2013. **85**(24): p. 11695-11699.
66. Choi, J., H. Lee, and S.J. Kim, *Hierarchical micro/nanoporous ion-exchangeable sponge.* Lab on a Chip, 2020.
67. Lee, J.H., et al., *Poly (dimethylsiloxane)-based protein preconcentration using a nanogap generated by junction gap breakdown.* Analytical chemistry, 2007. **79**(17): p. 6868-6873.
68. Kim, S.M., M.A. Burns, and E.F. Hasselbrink, *Electrokinetic protein*

preconcentration using a simple glass/poly (dimethylsiloxane) microfluidic chip. Analytical Chemistry, 2006. **78**(14): p. 4779-4785.

69. Martinez, A.W., S.T. Phillips, and G.M. Whitesides, *Three-dimensional microfluidic devices fabricated in layered paper and tape.* Proceedings of the National Academy of Sciences, 2008. **105**(50): p. 19606-19611.
70. Phan, D.-T., et al., *Sample concentration in a microfluidic paper-based analytical device using ion concentration polarization.* Sensors and Actuators B: Chemical, 2016. **222**: p. 735-740.
71. Hong, S., R. Kwak, and W. Kim, *based flow fractionation system applicable to preconcentration and field-flow separation.* Analytical chemistry, 2016. **88**(3): p. 1682-1687.
72. Martinez, A.W., et al., *Patterned paper as a platform for inexpensive, low□volume, portable bioassays.* Angewandte Chemie International Edition, 2007. **46**(8): p. 1318-1320.
73. Han, S.I., et al., *Microfluidic paper-based biomolecule preconcentrator based on ion concentration polarization.* Lab on a Chip, 2016. **16**(12): p. 2219-2227.
74. Gong, M.M., et al., *Nanoporous membranes enable concentration and transport in fully wet paper-based assays.* Analytical chemistry, 2014. **86**(16): p. 8090-8097.
75. Chang, H.-K., E. Choi, and J. Park, *Paper based energy harvesting from salinity gradients.* Lab on a Chip, 2016. **16**(4): p. 700-708.
76. Li, T., et al., *A nanofluidic ion regulation membrane with aligned cellulose nanofibers.* Science advances, 2019. **5**(2): p. eaau4238.
77. Nune, S.K., et al., *Green nanotechnology from tea: phytochemicals in tea as building blocks for production of biocompatible gold nanoparticles.* Journal of materials chemistry, 2009. **19**(19): p. 2912-2920.
78. Katti, K., et al., *Green nanotechnology from cumin phytochemicals: generation of biocompatible gold nanoparticles.* International Journal of Green Nanotechnology: Biomedicine, 2009. **1**(1): p. B39-B52.
79. Li, S., J. Hao, and M. Liddell, *Electrotransport across membranes in biological media: Electrokinetic theories and applications in drug delivery.* Transport in Biological Media, 1st ed.; Becker, S., Kuznetsov, A., Eds, 2013.
80. Manda, P., et al., *Iontophoresis across the proximal nail fold to target drugs to the nail matrix.* Journal of pharmaceutical sciences, 2012. **101**(7): p. 2392-2397.
81. Chopra, P., J. Hao, and S.K. Li, *Iontophoretic transport of charged macromolecules across human sclera.* International journal of pharmaceutics, 2010. **388**(1-2): p. 107-113.
82. Narasimha Murthy, S., D.E. Wiskirchen, and C. Paul Bowers, *Iontophoretic drug delivery across human nail.* Journal of pharmaceutical sciences, 2007. **96**(2): p. 305-311.
83. Baswan, S.M., et al., *Size and charge dependence of ion transport in human nail plate.* Journal of pharmaceutical sciences, 2016. **105**(3): p. 1201-1208.
84. Hao, J. and S.K. Li, *Transungual iontophoretic transport of polar neutral and positively charged model permeants: effects of electrophoresis and electroosmosis.* Journal of pharmaceutical sciences, 2008. **97**(2): p. 893-905.
85. Murthy, S.N. and H.I. Maibach, *Topical nail products and ungual drug delivery.* 2012: CRC press.
86. Probstein, R.F., *Physicochemical hydrodynamics: an introduction*. 2005: John Wiley & Sons.
87. Oh, Y., et al., *Capillarity ion concentration polarization for spontaneous biomolecular preconcentration mechanism.* Biomicrofluidics, 2016. **10**(1): p. 014102.
88. Rubinstein, I. and B. Zaltzman, *Equilibrium electroconvective instability.* Physical review letters, 2015. **114**(11): p. 114502.
89. Rubinstein, I., B. Zaltzman, and I. Lerman, *Electroconvective instability in*

concentration polarization and nonequilibrium electro-osmotic slip. Physical review E, 2005. **72**(1): p. 011505.

90. Moya, A., E. Belashova, and P. Sistat, *Numerical simulation of linear sweep and large amplitude ac voltammetries of ion-exchange membrane systems.* Journal of Membrane Science, 2015. **474**: p. 215-223.
91. Kwon, S., H. Lee, and S.J. Kim, *Elimination of pseudo-negative conductance by coercive steady state in perm-selective ion transportation.* Biomicrofluidics, 2020. **14**(1): p. 014106.
92. Sohn, S., et al., *Surface conduction in a microchannel.* Langmuir, 2018. **34**(26): p. 7916-7921.
93. Park, S. and R. Kwak, *Microscale electrodeionization: In situ concentration profiling and flow visualization.* Water research, 2020. **170**: p. 115310.
94. Cwirko, E.H. and R. Carbonell, *Transport of electrolytes in charged pores: analysis using the method of spatial averaging.* Journal of colloid and interface science, 1989. **129**(2): p. 513-531.
95. Rubinstein, I. and L. Shtilman, *Voltage against current curves of cation exchange membranes.* Journal of the Chemical Society, Faraday Transactions 2: Molecular and Chemical Physics, 1979. **75**: p. 231-246.
96. 이효민, *파상형 이온 선택 표면상의 전기와류 불안정성.* Korean Chem. Eng. Res.(화학공학), 2019. **57**(5): p. 735-742.
97. Druzgalski, C., M. Andersen, and A. Mani, *Direct numerical simulation of electroconvective instability and hydrodynamic chaos near an ion-selective surface.* Physics of Fluids, 2013. **25**(11): p. 110804.
98. Dhopeshwarkar, R., et al., *Transient effects on microchannel electrokinetic filtering with an ion-permselective membrane.* Analytical chemistry, 2008. **80**(4): p. 1039-1048.
99. Elizalde, E., et al., *Inverse problem of capillary filling.* Physical review letters, 2014. **112**(13): p. 134502.
100. Huang, Y.-R., et al., *Polymer nanocomposite films with extremely high nanoparticle loadings via capillary rise infiltration (CaRI).* Nanoscale, 2015. **7**(2): p. 798-805.
101. Gruener, S., et al., *Capillary rise of water in hydrophilic nanopores.* Physical Review E, 2009. **79**(6): p. 067301.
102. Bocci, V., *Albumen-gel as a supporting medium in zone electrophoresis.* Experientia, 1964. **20**(4): p. 234-235.
103. Zhao, L., *Egg albumen-a promising material for fabrication of nanoporous mats.* Thermal Science, 2016. **20**(3): p. 1014-1015.
104. Aguilar, J., et al., *Heat-induced gelation of egg yolk as a function of pH. Does the type of acid make any difference?* Food hydrocolloids, 2019. **87**: p. 142-148.
105. Kim, J., et al., *Pseudo 1-D Micro/Nanofluidic Device for Exact Electrokinetic Responses.* Langmuir, 2016. **32**(25): p. 6478-6485.
106. Kim, J., et al., *Ion concentration polarization by bifurcated current path.* Scientific reports, 2017. **7**(1): p. 1-12.
107. Phillips, G.O. and P.A. Williams, *Handbook of food proteins*. 2011: Elsevier.
108. Roozbahani, M.M., R. Borela, and J.D. Frost, *Pore size distribution in granular material microstructure.* Materials, 2017. **10**(11): p. 1237.
109. Oster, G., *Dye binding to high polymers.* Journal of Polymer Science, 1955. **16**(82): p. 235-244.

Abstract in Korean

이온선택성막은 해수담수화나 전기투석, 배터리등의 어플리케이션에 아주 광범위하게 활용되고 있다. 또한 이론적으로는 이온선택성 막 주변에서 일어나는 마이크로/나노 전기수력학적인 현상들에 대한 많은 보고가 있었다. 특히 이온선택성 막의 특성을 변경하는 것은 새로운 물리적 현상을 보여주거나 쉬운 공정법을 제시한다는 점에 있어서 많은 연구가 이루어 지고 있는데, 크게 이온선택성 막의 내부 구조를 바꾸거나 외부 모양을 바꾸는 두가지로 나누어 볼 수 있다. 본 연구에서는 이온수화젤이나 생체유래물질을 이용하여 내부 구조를 바꾸었을 때 와 나피온막의 표면을 파상형으로 제작하여 외부 구조를 바꾸었을 때 발생하는 현상에 대해 나타내었다. 따라서 본 연구는 두 파트로 나뉘는데 하나는 내부 구조를 바꾼 것이고 하나는 외부 모양을 바꾼 것이다.

두번째 장에서는 이온수화젤이 모세관이온농도분극현상을 발생시키는 이온선택성 막으로써 제시되었다. 전세계적인 물부족 현상을 해결하기 위해 다양한 해수담수화 방법과 효율증대를 위한 연구들이 진행되어 왔다. 하지만 맹그로브와 같은 식물은 극대화된 효율을 활용하여 염수환경에서 살아남는다. 이러한 맹그로브의 담수화 기능에 영감을 받아 모세관 이온농도 분극현상이 자발적인 담수화 메커니즘으로써 제시되었다. 일반적인 전기동역학적인 이온농도 분극현상이 외부 전기장에 의해 구동되는 것과 달리, 수화젤 본연의 모세관 힘에의해 선택적 이온 수송을 만들어내면서 수화젤 주변에서 자발적으로 이온 농도 분극

현상이 발생한다. 이 모세관 이온농도분극현상은 이온의 표지로써 넣어준 형광물질을 외부 전기장없이 90%이상 줄어들게 하였다. 이러한 결과들은 모세관 이온농도분극현상이 외부 전원 없는 정수 시스템 시장에 도움이 될 것으로 기대된다.

세번째 장에서는 손톱과 같은 잘 알려진 생체 물질을 이용한 생분해성의 물질이 이온선택성 투과막으로써 제시되었다. 이온선택성 투과막을 만들기위한 대부분의 나노 공정은 복잡하거나 높은 수준의 청정단계를 필요로 하는 비싼 공정이다. 반면에 마이크로 유체 플랫폼에서는 이미 싸고 생체적합한 다양한 물질들이 이미 다양하게 연구되어 오고 있다. 따라서 생분해성의 이온선택성 투과막을 활용하면 친환경적인 마이크로/나노 유체 플랫폼의 개념을 완성시킬 수 있다. 간단한 마이크로/나노 장치가 제작되었고, 이온농도분극현상의 시각화, 옴영역, 한계영역, 과한계영역으로 대표되는 전류전압특성 그리고 포면전하 기반의 전도도등을 간단한 실험을 통해 밝혀냈다. 따라서 손톱과 같은 생체유래물질을 사용하면 환경친화적이면서도 생분해성인 마이크로 나노 장치에 적용할 수 있을거라 기대할 수 있다.

네번째 장에서는 파상형구조의 표면을 갖는 나피온 막이 포함된 마이크로/나노 유체 플랫폼이 제작되고 연구되었다. 특히 특성길이에 따른 전기동역학적인 효과들에 대해서 알아보았는데, 일반적인 파상형 구조의 표면을 갖는 연구들은 대부분 긴 특성길이 (~O(100) μm)에서 실험되고 해석 되어 온 반면, 본 연구에서는 짧은 특성길이 (~O(10) μm)에서의 효과 역시 실험하고 비교되었다. 특히 전류 전압 특성을 통해 파상형 구조의 효과가 짧은 특성길이에서 억제되는지를 살펴보았다.

본 연구에서는 이온선택성 투과막의 외부 모양이나 내부 구조를 변형하여 발생하는 새로운 현상이나 새로운 특징들에 대해 실험하고

보고 하였다. 두번째와 세번째 장에서는 새로운 내부구조를 활용한 이온선택성 투과막에 대해 연구하였고, 네번째 장에서는 외부 모양을 바꾸었을 때 일어나는 새로운 물리적 특징들에 대해 연구하였다. 본 논문을 통해 다양한 이온선택성 투과막에 대한 이해가 높아지고 더 다양한 연구들이 화발히 진행되기를 바란다.

주요어 : 이온농도분극현상, 이온선택성막, 이온수화젤, 손톱, 모세관힘, 파상형 표면

학번 : 2013-20791